Optical properties of metal nanoparticles investigated using polarised light.

Erik Vedeler

Master Thesis in Nano Science

Supervisors: Professor Dr. Bodil Holst
Dr. Martin Møller Greve
Co-supervisor: Ranveig Flatabø

Department of Chemistry
University of Bergen

April 2017

Acknowledgements

I would like to start by expressing my sincere gratitude to my supervisors Dr. Bodil Holst and Dr. Martin Møller Greve and Ranveig Flatabø for giving me the opportunity to work on this exciting project. Their guidance, input and understanding has been invaluable, and help was always readily available when needed. I would also like to thank the rest of the nanophysics group, which made the process a lot more enjoyable both in the form of social experiences and interesting discussions. Last but not least I wholeheartedly thank my friends and family for providing much needed support, this thesis could not have been completed without them.

Abstract

The number of applications of metal nanoparticles (MNPs) are growing, and one of their most interesting properties is the interactions between MNPs and light. Especially in the visible regime, MNPs are very good at absorbing light at specific wavelengths, which opens interesting opportunities for use in many technological branches ranging from quantum dot displays to solar energy conversion. The principle behind the light absorption is the localised surface plasmon (LSPR) effect, in which the oscillating electric field of the light wave excites the electrons of the particle. The resonance of these oscillations is dependent on the size, shape, metal type and surrounding medium of the particle, and as such these parameters can be tailored depending on the application. Because of the surrounding mediums effect on the resonance wavelength, nanoparticles can be used in sensors to detect changes in refractive index.

The goal of this thesis work is to investigate the viability of nanoparticle arrays as sensor devices, and more specifically explore a phenomenon in which the LSPR is selectively supressed to decrease the width of the plasmon peak, enhancing the sensitivity of potential sensor applications. Large arrays (1 x 1 mm) of gold nanoparticles with varying interparticle distances were fabricated using electron beam lithography (EBL), and the fabrication process was iteratively improved due to an initial lack of particle adhesion to the substrate surface, resulting in samples with a quality high enough to perform optical measurements. The particles were analysed by means of transmission spectroscopy, employing both polarised and unpolarised light, the former using a novel spectrometer. The measurements presented here are the first measurements carried out with polarised light at the UiB nanostructures laboratory. The results demonstrate the suppression of the LSPR, and the spectral positions of these suppression dips, as well as the relationship between the optical response of the particles when subjected to polarised light as compared to unpolarised light. This lays the foundation for further investigation into a refractive index sensor based on nanoparticles.

Table of contents

List of figures

List of tables

1 Introduction

1.1 Background

Nanoparticle fabrication and characterization has been of interest across multiple fields of study for a long time. Before they were characterized scientifically, artists unknowingly employed nanoparticles as colouring agents in their works, including the Lycurgus cup (Figure 2.1) and other glassworks. The particles were created by "*adding copper and silver salts together with vinegar, ochre and clay on the surface of previously glazed pottery. The object was then placed in a kiln and heated to approximately 600°C in a reducing atmosphere*" (Khan 2011, p. 328) [1]. The first modern description of the optical properties of nanoparticles were given by Faraday's investigations of colloidal gold particles, starting in 1857 when he discovered that gold can appear red when reduced to a nanometre scale [2][3]. One of the main driving forces of the interest in nanoparticles is the diverse amount of applications and physical phenomenon they exhibit.

In comparison to the behaviour of metals and alloys we know from our daily lives, for instance iron or gold, once they are reduced to the nanoscale size the properties change dramatically. The melting point, electrical and magnetic properties, colour and even chemical reactivity are demonstratively altered once the particles approaches the nano scale, which is defined as structures below 100 nm [4]. A good example of this is gold, which in its bulk form is known to be chemically unreactive; In nanoparticle form of very small sizes (> 5 nm, see Figure 1.3), gold is used as a very effective catalyst due to their high activity at comparatively low temperatures [5]. Another striking difference, as mentioned, between the gold that we are used to and gold in nanoparticle form is that the colour of the particles can change based on particle size or shape alone, as shown in Figure 1.1, see also [6].

Figure 1.1 Gold nanoparticles of sizes 5-100 nm. The particles selectively absorb light based on the particle size, which is why golden particles with diameters below 100 nm appears red rather than the gold colour we are used to from the bulk material. Picture taken from the nanoComposix website, a nanoparticle manufacturer [7].

One of the key concepts that allow these changes are the ratio of surface to volume in the particle. Imagine a cube of one cubic meter, where each of the cubes faces has an area of one square meter. The total surface area of this cube is six square metres. If we divide the cube into eight smaller cubes with side lengths of half a meter, the total surface area is doubled to twelve square metres while the volume is unchanged. This is because the surface that previously faced inward in the large cube is now exposed. In the case of nanoparticles, the cube has been divided a million times, meaning they exhibit a very large surface area compared to their volume. Most chemical and physical interactions happen on the surface of a material, and these interactions are therefore greatly enhanced in the case of nanoparticles [8].

The interactions between light and matter is also influenced by the particle size, and it is these interactions that are going to be investigated in this thesis. When making nanoparticles, there are two main branches of techniques that can be employed: The top-down, or bottom-up approach. As the name suggests, the top-down approach starts with a bulk material and "whittles" it down to the desired particle size, while the bottom-up approach builds the particles atom by atom or molecule by molecule. Based on these two underlying principles, many methods of fabrication have been created, and the method used in this work is a top-down based approach called electron beam lithography (described in detail in section 3.2). Using this method, particles can be created with nanometre precision, allowing the tailoring of particle size and shape.

1.2 Nanoparticle applications

As previously mentioned, matter with nanoscale dimensions tend to gain additional properties outside of what we can expect from the material in bulk form. Materials can exhibit different colours than what we are used to based on the particle size and shape, and the magnetic field of certain materials are suddenly enhanced once the particles become small enough. The following is a collection of the applications of these properties with the main emphasis on optical properties of nanoparticles, which is the topic of this thesis.

1.2.1 Magnetic properties

Iron is widely known to be a magnetic material, however pure iron is not magnetized [8]. Magnetism in materials comes from the atoms themselves, where the movement of electrons around the nuclei creates a magnetic moment, essentially turning each atom into a permanent dipole magnet. In ferromagnetic materials, these magnetic dipoles influence their neighbouring atoms, creating what is known as magnetic "domains", which are groups of atoms with the same magnetic orientation. In a magnet as we know it, these domains are separated by a nonmagnetic material so that the domains can align in the same direction. A nanoparticle can be so small that it is comparable to the size of these domains (for iron this is about 100 nm [8]), and this is the reason why iron nanoparticles are much more ferromagnetic than its bulk counterpart.

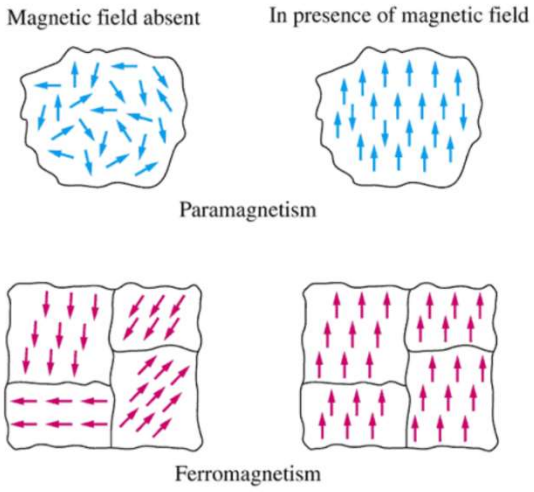

Figure 1.2 Illustration of magnetic domains. Note the distribution of the magnetic moment directions in the paramagnetic material in presence of a magnetic field; there is an equal amount of each dipole direction, resulting in zero net magnetic field. Figure reproduced from [9].

These magnetic nanoparticles have seen a variety of applications, the most prominent one arguably being in the medical field with a potential cancer treatment called magnetic hyperthermia. The underlying principle of this treatment method is to attach the magnetic nanoparticle to a ligand that is absorbed by the cancer cell, and once absorbed the particle is subjected to a rapidly oscillating magnetic field. This causes the particle to heat up, which kills the cancer cell [10]. Another potential use for magnetic nanoparticles are in digital storage, where the small particle size and distinct magnetic field potentially allows for very space-efficient hard disks [11].

1.2.2 Chemical properties

As briefly mentioned, nanoparticles have been used to facilitate chemical reactions by acting as a catalyst. One of the most dramatic examples of this is found in gold, where the bulk material is notoriously unreactive. As such it does not tarnish or corrode, which is part of the reason why it is so highly valued. However, the chemical properties of gold drastically changes once it is reduced to particles of about 5 nm [12]. At this size, gold particles become a powerful catalyst, especially for the oxidation of carbon monoxide molecules (CO). As shown in Figure 1.3, the reactivity of the particles increase exponentially with decreasing size. The reason for this is that only surface atoms can contribute to catalysis, and surface area per particle volume increases with decreasing particle diameter. Gold has been used as an example because of its transformation from an inert material to a reactive one simply by altering particle size, however this also applies to the performance of all catalysts [8].

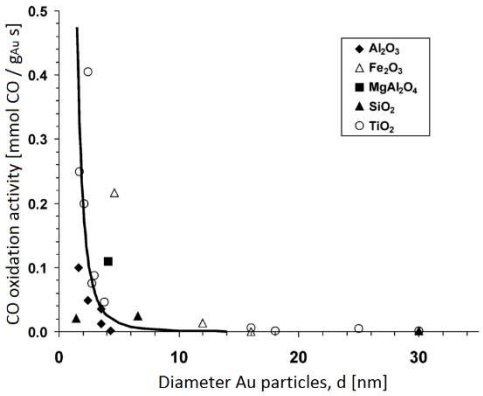

Figure 1.3 Oxidation reactivity of gold nanoparticles. The different indicators correspond to the material supporting the gold particles. This also affects the reactivity, however [12]*, from which this figure is reproduced, concluded that particle size is the dominant factor. The solid line is a $1/d^3$ approximation to the reactivity, which is considered a rule of thumb.*

1.3 Optical properties of nanoparticle investigations

The most prominent optical interactions between light and nanoparticles are their ability to scatter and absorb light. These interactions are governed by the particles size, shape, and the medium in which the particles are situated. When the oscillating electric field of a light wave interacts with a metal nanoparticle, the conduction electrons are displaced by the field. At a certain frequency these oscillations are resonant, and it is at this frequency where the particle absorption and scattering is at its maximum. This effect is called the excitation of a localized surface plasmon (LSP), and is described in detail in detail in section 2.2. When the resonance frequency (LSPR) lies within the visible spectrum, the particles exhibit vibrant colours, and the colour type is decided by the resonance. As such, the colour of the particle can be fine-tuned by changing either the particle size, shape or the surrounding medium. This tuneable light absorption can be very beneficial to a number of industries, for instance sensors, solar cells and electronics.

1.3.1 Electronics

In electronics, one of the challenges the industry is facing is the ever-decreasing size of components. The diffraction limit states that electromagnetic radiation cannot be confined in an area smaller than half of the radiations wavelength, which introduces a physical limit to the size of the electronic components. One possible solution to this is to decrease the wavelength used, however this means increasing the photon energy which not only would increase energy consumption of the system, but could also compromise the longevity of the components due to heat exposure. With nano-particles, this problem can be circumvented by the LSPR effect, with which it is possible to squeeze the light into regions below the diffraction limit [13].

1.3.2 Solar cells

The LSPR effect is also central to the application of nanoparticles in solar cells. The solar industry is currently dominated by semiconductor based photovoltaic cells, in which the light is absorbed by exciting electrons from the valence band into the conduction band of the semiconductor. This is called the photoelectric effect, and is the basis of all photovoltaic cells. One of the drawbacks of this method is that the bandgap of the semiconductor, which is the energy required to excite an electron from the valence to the conduction band, is inherently reducing the effectiveness of the light absorption. This is because the photons with a lower

energy than the bandgap does not contribute to the generated electric energy at all due to the lack of excited electrons, and in the case of photons with an energy greater than the bandgap the excess energy are lost as heat. As such, the maximum theoretical absorption efficiency of a single junction semiconductor solar cell is 33.7% [14]. To improve the existing semiconductor based technology, nanoparticles has been employed as absorbers to enhance the efficiency of the cell using the LSPR effect. The light emitted from the sun has its intensity peak in the visible range [15], and the particles geometry can be tailored so that the LSPR spectral position coincides with the visible light frequencies. There is also ongoing research into utilizing particles by themselves without a semiconductor setup, however at present this technique can only transform the solar energy to heat, and a secondary conversion must take place in order to output electrical energy [16]. In the work of Eidsvåg [17], a combination of particles with different diameters was used in an attempt to absorb as much of the visible spectrum as possible, demonstrating the possibilities for tailor-made solar absorbing structures.

1.3.3 Nanoparticle based sensors

The LSPR spectral position is influenced by the refractive index of its surrounding medium, as detailed in section 2.4.1. As such, changing the refractive index of the medium will shift the LSPR peak. This is the basis of a sensor based on nanoparticles, and has been studied extensively, and produced very accurate sensors that in some cases can detect single molecules based on the spectral shift of the LSPR [18]. The sensitivity of such sensors depend on how accurately the spectral shifts can be measured, which is why the goal is to manufacture particles with a well-defined plasmon peak. A common way to quantify the quality of the plasmon peak is the “figure of merit” (FOM) parameter

$$FOM = \frac{1}{\Delta\lambda}\frac{d\lambda_{sp}}{dn} \qquad (1.1)$$

where λ_{sp} is the resonance wavelength, n is the refractive index, and $\Delta\lambda$ is the linewidth (sometimes referred to as full width at half maximum, or FWHM). Yong et al. [19] conducted a study comparing the FOM values of particles with several different geometries, and reported a linewidth ranging from 278.6 (nanorod with a small aspect ratio, FOM 2.6) to 91.7 nm (nanobipyramid, FOM 7.4), and drew the conclusion that irregular shapes, in particular those containing sharp tips, led to the highest sensitivity. This is however a trade-off between sensor

sensitivity and fabrication difficulties, as it is much harder to consistently produce such structures in comparison to spheres. Despite spheres being perceived inferior for sensing purposes, Liu et al. [20] presented a near perfect absorber made using electron beam lithography, consisting of gold nanodisks with a diameter of 352 nm and a height of 20 nm. At resonance, these nanodisks reach an experimental absorbance of 99%. When subjected to different mediums (water and glucose of refractive indices of 1.322-1.352) the calculated FOM reached 87. The linewidth used in the calculation was not provided, but based on the figures it was about 40 nm. This indicates that it is the absorbing properties of the particles that is key to obtain a high FOM.

Equation 1.1 shows that another important factor to achieving a high FOM is the linewidth of the excited plasmon curve. Linden et al. [21] reported a phenomenon in which nanoparticles situated in a regular grid on top of an indium tin oxide (ITO) waveguide led to suppression of the plasmon at select spectral positions. The result of this was a small peak in the middle of the plasmon situated between two sites of suppression (see Figure 1.4) with an approximate linewidth of 20 nm. This is even lower than the linewidth of the near perfect absorber created by Liu et al. Based in these findings, it should be possible to manufacture such a system that ultimately could be suitable for sensing changes in refractive index.

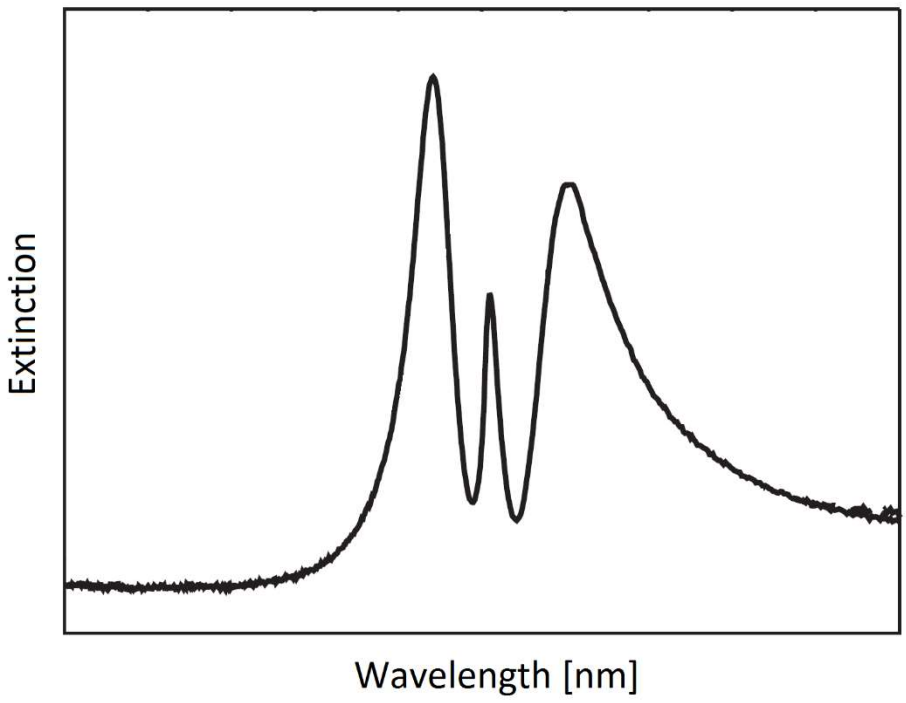

Figure 1.4 Sketch of the suppressed plasmon curve. An LSPR has the shape of a single, broad peak. When nanoparticles are situated in a periodic array on a waveguide, this single peak is suppressed at two different wavelengths, creating a thin peak between them. Redrawn from [21].

1.4 Thesis Objective

The aim of this thesis is to further investigate the selective suppression of the plasmon resonance that occurs when gold nanoparticles are situated on a conduction waveguide (ITO). The ultimate goal is to apply the effect in sensor applications. This will be performed as follows:

- A collection of gold nanoscale spheres will be manufactured on a substrate of glass covered by an ITO film, by means of electron beam lithography.
- These samples will be analysed using transmission spectroscopy with polarised light, in order to correlate the effects of polarisation to the optical response of the particles.
- Based on the analysis, determine if the design is feasible for creating a nanoparticle based sensor.

1.5 Thesis Outline

Chapter 2 presents a theoretical background of the surface plasmon resonance effect, the spectroscopy technique, and the coupling of light into a nanoscale waveguide. Chapter 3 gives an overview of the experimental equipment used in particle fabrication and optical analysis. The iterative process of manufacturing the particles is described in chapter 4, starting with previously established methods and the alterations made along the way. Chapter 5 presents the results and discussion of the optical measurements carried out, and chapter 6 provides a conclusion and suggestion for further work.

2 Theoretical Background: Selective Suppression of the Localized Surface Plasmon.

2.1 The Field of Plasmonics

A plasmon is the collective displacement of electrons influenced by an external electric field, and the study of such effects has been named plasmonics. The term “plasmon” refers to an oscillation of the electron plasma surrounding the positive nuclei in a metal, and was coined by Pines in 1956 [22]. Technological advancements in the fabrication of nanostructures and a wide range of potential applications has led to an increasing interest in the research of plasmons in recent years, but the plasmonic effect was first observed back in Roman times, where glassmakers unknowingly used nanoparticles to stain glass. The perhaps most famous example of this is the Lycurgus cup, which was made around the 4th century. This cup appears to be green when light is reflected from the surface, but if light is transmitted through the cup it appears red. We now know that the cause of this effect is the interactions between light the gold and silver alloy nanoparticles in the glass [23].

(a) **(b)**

Figure 2.1 The Lycurgus cup. Figure a shows the cup when light is reflected back to the observer, while b shows light transmitted through the cup. Pictures taken from [23].

The particular phenomenon that caused the particles in this cup to display such colouring is the localized surface plasmon (LSPR), which is one of the two major types of plasmons considered in the field of plasmonics, the other being the volume plasmon. One of the interesting properties of the LSPR is that it exhibits an electric field contained at a much smaller distance than the wavelength of the light used to excite it; you can utilize LSPRs to contain light at regions below the theoretical diffraction limit defined at about half the light's wavelength.

The LSPRs excited from metal spheres were described mathematically at the beginning of the 19th century by Mie in 1908 [24], where he presented an exact solution to Maxwell's equation that describes the scattering and absorption of electromagnetic radiation by a sphere. A few years prior, in 1902, Wood [25] discovered "anomalous" intensity drops when visible light passed through metallic gratings. This turned out to be due to the excitation of plasmons, but that was not realized until the work of Fanø [26] in 1941. In 1957, Ritchie [27] used fast electrons hitting a thin metallic film to demonstrate plasmons on a metal surface. Kreibig and Zacharias [28] applied this theory to nanostructures, and in 1970 they described the optical response of silver and gold nanoparticles in terms of plasmons.

2.2 Interactions between metals and light

The interactions between metals and electromagnetic radiation can, in the classical realm, be described using Maxwell's four equations[29]:

$$\nabla \cdot \boldsymbol{D} = \rho \tag{2.1}$$

$$\nabla \cdot \boldsymbol{B} = 0 \tag{2.2}$$

$$\nabla \times \boldsymbol{E} = -\frac{\partial \boldsymbol{B}}{\partial t} \tag{2.3}$$

$$\nabla \times \boldsymbol{H} = \boldsymbol{J} + \frac{\partial \boldsymbol{D}}{\partial t} \tag{2.4}$$

Where **D** is the dielectric displacement, **B** is the magnetic flux density, **E** is the electric field and **H** is the magnetic field. These are the four macroscopic fields. **J** and ρ are the external current and charge densities. If we limit the discussion to linear, isotropic and nonmagnetic materials, one can define some constitutive relations between these fields. A constitutive

relation governs the response of a specific material to external stimuli, which in this case describes how the different fields are acting on one another:

$$\boldsymbol{D} = \varepsilon_0 \varepsilon \boldsymbol{E} \quad (2.5)$$

$$\boldsymbol{B} = \mu_0 \mu \boldsymbol{H} \quad (2.6)$$

$$\boldsymbol{J} = \sigma \boldsymbol{E} \quad (2.7)$$

ε_0 and μ_0 are the electric permittivity and magnetic permeability of vacuum respectively, which are constant. Finally, the dielectric displacement and the electric field are linked by the polarization **P** [29]

$$\boldsymbol{D} = \varepsilon_0 \boldsymbol{E} + \boldsymbol{P} \quad (2.8)$$

These relations can be used to obtain a mathematical description of the dielectric constant, with the help of the free electron model.

2.2.1 The free electron model

The optical properties of metals can be described by modelling them as a background of positive ion cores with a "sea" of free electrons floating on top. This model was proposed by Drude [30] in 1900, only 3 years after J.J. Thomson discovered the electron, and builds on the assumption that the free electrons behave like an ideal gas. This means that we assume no interactions between the electrons, neither coulomb nor collisions. They can however collide with the positive ion cores, but in between collisions no other interactions are present. These collisions are responsible for the thermal equilibrium of the system, which according to the equipartition theorem is [31]

$$\frac{1}{2} m_e v_t^2 = \frac{3}{2} k_B T \quad (2.9)$$

This yields an average velocity of about 10^5 m/s in room temperature. The average length that an electron moves in between collisions depends on the density of the ion cores. This distance is called the mean free path of the electron, and is typically $\lambda \approx 1\ nm$ [31]. Knowing the speed

and length, we can calculate the time between each collision called the relaxation time $\tau \approx 1\times10^{-14}\ s$, which in turn yields the characteristic collision frequency of $\gamma = \frac{1}{\tau} \approx 100\ THz$ [29]. This collision frequency describes the dampening of the electron motion.

2.2.2 The dielectric function

We can use the free electron model to obtain a mathematical expression of the dielectric constant. Starting with a simple motion equation of the electrons in the plasma [29]

$$m\frac{\partial^2 \boldsymbol{x}}{\partial t^2} + m\gamma\frac{\partial \boldsymbol{x}}{\partial t} = -e\boldsymbol{E}(t) \qquad (2.10)$$

where m is the electron mass, x is the displacement of electrons and e is the electron charge. We now utilize the following:

- We assume a harmonic time dependence, $\boldsymbol{E}(t) = \boldsymbol{E}_0 e^{-i\omega t}$, which when combined with equation 2.10 yields a particular solution of $\boldsymbol{x}(t) = \boldsymbol{x}_0 e^{-i\omega}$
- The macroscopic polarization is defined as $\boldsymbol{P} = -ne\boldsymbol{x}$, where n is the density of the electron gas. This density is defined by the number of electrons in the outermost shell of the metal atom [31].
- We define the plasma frequency of the free electron gas as $\omega_p^2 = \frac{ne^2}{\varepsilon_0 m}$

Applying this to equation 2.10 and combining it with equation 2.8 and 2.5, we arrive at the dielectric function of a free electron gas [29].

$$\varepsilon(\omega) = 1 - \frac{\omega_p^2}{\omega^2 + i\gamma\omega} \qquad (2.11)$$

The dielectric constant is directly related to the refractive index, where $n = \sqrt{\epsilon}$. When the frequency of the electromagnetic waves that interact with the metal are larger than the plasma frequency, that is $\omega < \omega_p$, the dielectric constant becomes negative. Consequently, the refractive index will be imaginary, implying that the radiation cannot propagate through the

metal. This is indeed the case, and electromagnetic radiation below the plasma frequency will be reflected when it encounters the metal surface. When $\omega > \omega_p$, the dielectric constant becomes real, which implies that the electromagnetic wave is partially propagating through the metal. This transition happens in the ultra violet frequency range for most metals, and visible light is therefore reflected.

While this model agrees quite well with experiments for most metals, there are some exceptions. Most notably in this work, some metals like copper and most noble metals have electronic interband transitions in the visible frequency spectrum, which absorbs distinct energy wavelengths. This effect can however be accounted for by adding an electron resonance frequency term to equation 2.10 [29].

2.3 Surface plasmon polaritions

Now that we have a description of how metals interact with an oscillating electric field such as a ray of light, we can move on to describing the waves of displaced electrons that occurs when the plasma is excited along a metal surface in a dielectric environment. These waves are called surface plasmon polaritions. We start with the central equation of electromagnetic wave theory [29]

$$\nabla^2 \boldsymbol{E} - \frac{\varepsilon}{c^2}\frac{\partial^2 \boldsymbol{E}}{\partial t^2} = 0 \qquad (2.12)$$

We also, like in the previous section, assume a harmonic time dependence, which turns equation 2.12 into

$$\nabla^2 \boldsymbol{E} + k_0^2 \varepsilon \boldsymbol{E} = 0 \qquad (2.13)$$

where k_0 is the wave vector propagating through vacuum, defined as $\frac{\omega}{c}$. We then assume that the surface plasmon polarition (SPP) is propagating in the x-direction. The x-component of the wave vector is named $\beta = k_x$. This is known as the propagation constant, and by using the curl equations (2.3 and 2.4) we can calculate the dispersion relation of a plasmon propagating between two half spaces, one metal and one dielectric. This relation is given by [29]

$$\beta = k_0 \sqrt{\frac{\varepsilon_1 \varepsilon_2}{\varepsilon_1 + \varepsilon_2}} \qquad (2.14)$$

Here ε_1 and ε_2 are the dielectric constants of the conductor (metal) and the dielectric, respectively. If we use some example media like air and fused silica, we can plot this relation graphically.

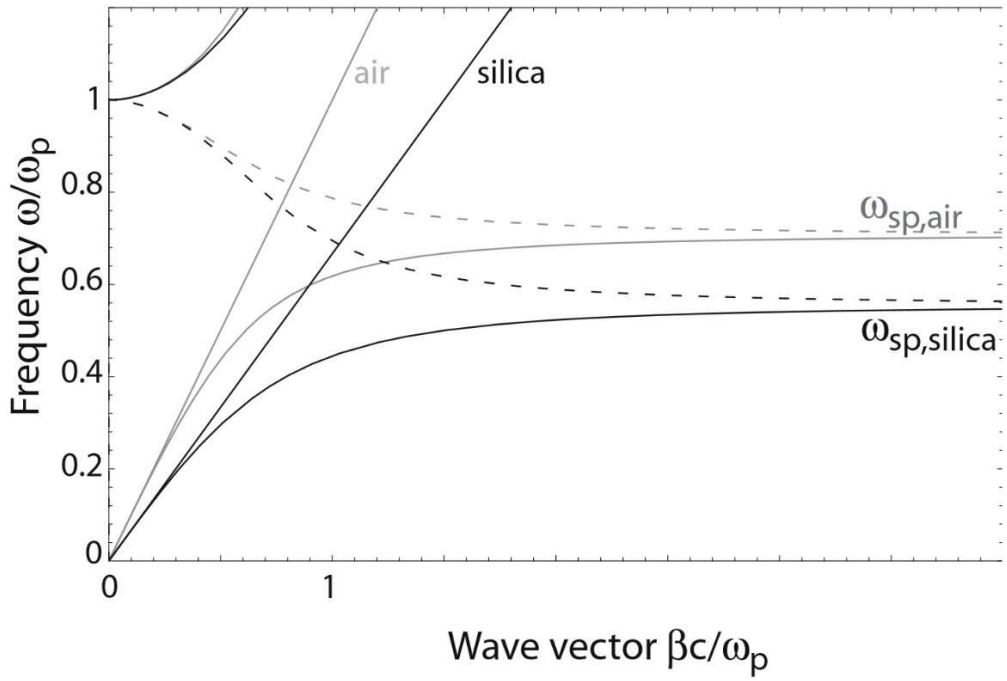

Figure 2.2 Dispersion relation between air and fused silica. The dielectric constants of air and silica are 1 and 2.25 respectively. Figure taken from [29].

As we can see, the curves of the propagation constants β are to the right of their respective light lines. This means that the frequency, and therefore also the momentum of the propagating plasmon must be larger than the momentum of the electromagnetic radiation used to excite it. This cannot be the case because momentum is conserved, and consequentially SPPs cannot be directly excited on a metal-dielectric interface using radiation alone. Special phase matching techniques are required, such as prism- or grating coupling. This enables us to shift the β-curves to the left, making excitation possible. Once excited, the SPP propagates along the metal surface and is dampened by interactions between the free electrons and by interband transitions. The perpendicular field that propagates out in the dielectric is evanescently confined, and given by the z-component of the wave used to excite the polarition $\hat{z} = \frac{1}{|k_z|}$. A typical trade-off with SPPs

is that the better the confinement in the z-direction, the larger the propagation distance. The confinement can also go below the diffraction limit, which has many interesting applications in optical and sensing devices [32].

2.4 Localized surface plasmons

While we cannot excite plasmons directly on a metal surface, the situation changes when the metal is shaped as small particles. Specifically, if the particles are considerably smaller than the wavelength of the incident electromagnetic wave, the electrical field of the light wave can be considered uniform across the whole particle. This is called the *quasi-static approximation*. When this is the case, the electric field can displace the conduction electrons of the particle, creating a potential between the electrons and the positive ion cores of the metal atoms. This potential difference causes a restoring force to act on the displaced electrons, pulling them back to their original position. These oscillating electron clouds are called localized surface plasmons (LSPs)

2.4.1 LSP resonance condition

The separation of charges enables an approximation to the response of the particle to that of an oscillating dipole, and for a certain frequency of light these oscillations will be resonant.

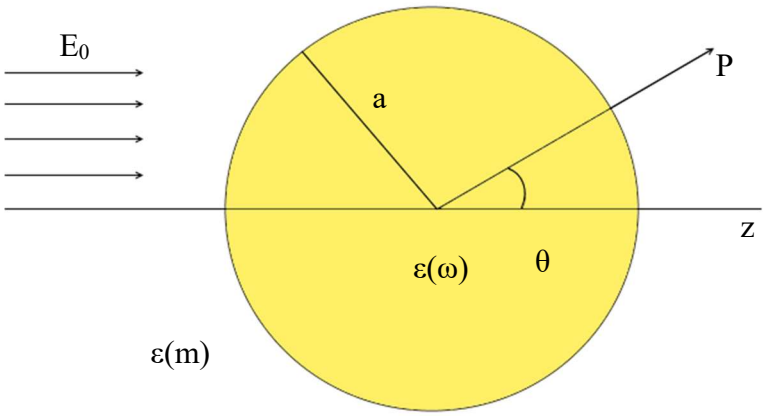

Figure 2.3 Illustration of particle placed in an electrostatic field. E_0 is the electric field from the incident light. ε(m) and ε(ω) is the dielectric constants of the medium around the particle and the metal, respectively.

The optical response from a spherical metal particle (illustrated in Figure 2.3) with a diameter much smaller than the wavelength of the incident light field can be calculated by solving the LaPlace equation

$$\nabla^2 \Phi = 0 \qquad (2.15)$$

Which we can use to calculate the electric field

$$\boldsymbol{E} = -\nabla \Phi \qquad (2.16)$$

The particle is assumed to be a homogenous isotropic sphere which is in the origin of a uniform, static electric field $\boldsymbol{E} = E_0 \vec{z}$. The particular solution to equation 2.15 inside and outside the particle is [29]

$$\Phi_{in} = -\frac{3\varepsilon_m}{\epsilon + \epsilon_m} E_0 r \cos\theta \qquad (2.17)$$

$$\Phi_{out} = -E_0 r \cos\theta + \frac{\varepsilon - \varepsilon_m}{\varepsilon + 2\varepsilon_m} E_0 a^3 \frac{\cos\theta}{r^2} \qquad (2.18)$$

where ε and ε_m is the dielectric constants of the medium surrounding the particle, and the metal respectively. Φ_{out} describes the superposition of the driving field E_0 and a dipole located in the centre of the particle. If we introduce a dipole moment **p**

$$\boldsymbol{p} = 4\pi\varepsilon_0\varepsilon_m a^3 \frac{\varepsilon - \varepsilon_m}{\varepsilon + 2\varepsilon_m} \boldsymbol{E}_0 \qquad (2.19)$$

where ε_0 is the permittivity of vacuum. Combining equation 2.18 and 2.19, we can rewrite Φ_{out} as

$$\Phi_{out} = -E_0 r \cos\theta + \frac{\boldsymbol{p} \cdot \boldsymbol{r}}{4\pi\varepsilon_0\varepsilon_m r^3} \qquad (2.20)$$

In other words, the driving field induces a dipole moment inside the particle that is proportional to $|\mathbf{E}_0|$. This dipole moment can be expressed using the polarizability α

$$\boldsymbol{p} = 4\pi\varepsilon_0\varepsilon_m \alpha \boldsymbol{E}_0 \qquad (2.21)$$

When combining equation 2.19 and 2.21 we get the polarizability of a small metal sphere influenced by a static electric field

$$\alpha = 4\pi a^3 \frac{\varepsilon - \varepsilon_m}{\varepsilon + 2\varepsilon_m} \quad (2.22)$$

The polarizability α is in other words dependent on the relationship between the dielectric constants in the metal and medium. It is at its peak when the denominator of equation 2.22 is at its minimum

$$\varepsilon = -2\varepsilon_m \quad (2.23)$$

which is called the Frölich condition [29]. The frequency that satisfies this condition is where the localized surface plasmon resonance (LSPR) will occur. Due to the fact that the dielectric constant is a complex number (see equation 2.11), the polarization does not approach infinity at resonance, because the imaginary part does not equal to zero. The Frölich condition shows that you can alter the spectral position of the LSPR by changing the dielectric constant of the medium surrounding the particle, which has been investigated by numerous studies [33]. Once the LSPR has been excited, the resulting oscillating dipole causes scattering of the incident light wave. As such the particle both absorbs and scatters the light, and the probability of that happening is described by the absorption and scattering cross sections

$$C_{sca} = \frac{k^4}{6\pi}|\alpha|^2 = \frac{8\pi}{3}k^4a^6\left(\frac{\epsilon - \epsilon_m}{\epsilon + 2\epsilon_m}\right)^2 \quad (2.24)$$

$$C_{abs} = kIm[\alpha] = 4\pi ka^3 Im\left[\frac{\varepsilon - \varepsilon_m}{\varepsilon + 2\varepsilon_m}\right] \quad (2.25)$$

where $k = \frac{2\pi}{\lambda}$ is the wavenumber. One of the interesting properties of this result is that the absorption and scattering of the particles scale differently with increasing particle size. As a general rule, small particles (< 50 nm) is more absorbing, and particles larger than this are mainly scattering. This is the reason why particles of different sizes exhibit different colours [29].

2.5 Spectroscopy

The basis of spectroscopy is to investigate the interactions between light and matter. In this work, two different spectrometers were used: The Filmetrics thin film analyser (TFA, described in section 3.4) and a transmission spectrometer (TS, described in section 0). The main difference between the two is that the TS is equipped with a polarisation filter, while the TFA has an unpolarised light source. In both cases, the incident light is normal to the sample surface. The objective of the measurements is to identify the extinction of the MNPs, which is defined by the sum of the scattering and absorbing cross sections as described in equations 2.24 and 2.25 [34]. The extinction can be related to the absorbance A of the sample by using Beer-Lamberts law [29].

$$A(\lambda) = \alpha_{ext}\tau \quad (2.26)$$

where α_{ext} is the absorption coefficient and τ is the optical path length. The term that relates this expression to the extinction cross section is α_{ext}, which can be defined as [34]

$$\alpha_{ext}(\lambda) = f\big(C_{sca}(\lambda) + C_{abs}(\lambda)\big) = fC_{ext}(\lambda) \quad (2.27)$$

Where f is a volume filling factor (Beer-Lamberts law is usually applied to liquids or gases). The terms absorbance and extinction has been used interchangeably [35], and as such we can write

$$Extinction = Absorbance = -\log T(\lambda) \quad (2.28)$$

The transmittance T is the ratio between transmitted and incident light, defined as

$$T(\lambda) = \frac{I_t(\lambda)}{I_0(\lambda)} \quad (2.29)$$

where T is the transmittance, I_0 is the incident light intensity and I_t is the intensity of the light transmitted through the sample. In order to accurately obtain these measurements in practice, the intensities were corrected for their respective background spectrums, which measures the spectrum when the light source is off in order to correct for background lighting. Thus, the complete transmission calculation is

$$T(\lambda) = \frac{I_t(\lambda) - I_b(\lambda)}{I_0(\lambda) - I_b(\lambda)} \quad (2.30)$$

where I_b is the background spectrum. These calculations were performed two times for each sample, one with the light source shining on the particles themselves, and one where only the substrate transmittance was measured. The difference between these two spectrums represent the extinction of the MNPs.

$$Extinction_{MNPs} = Extinction_{sample} - Extinction_{substrate} \quad (2.31)$$

2.6 Coupling of light into waveguides

An optical waveguide is a physical structure through which light can propagate. In the samples produced in this thesis, the waveguide consists of a 300 ± 20 nm layer of indium tin oxide (ITO) which is deposited on top of a borosilicate glass coverslip. ITO is a semiconductor with a bandgap of 3.5-4.3 eV (depending on the method of fabrication and film thickness), that exhibits a high transmittance of visible light; Diamond coatings, the producer of the substrates, informs that the ITO layer exhibits a transmittance of more than 70% across the visible spectrum, peaking at 88% for wavelengths around 550 nm. When coupling light into the ITO-layer, it is important that the light frequency exceeds the cut-off frequency. The cut-off frequency is the lowest frequency for which a mode will propagate in a waveguide. This is defined as [21]

$$\omega_{cut} = \frac{c\ tan^{-1}\left(\sqrt{\frac{\varepsilon_{Sub} - \varepsilon_{Air}}{\varepsilon_{ITO} - \varepsilon_{Sub}}}\right)}{d\sqrt{\varepsilon_{ITO} - \varepsilon_{Sub}}} \quad (2.32)$$

where ω_{cut} is the cut-off frequency, c is the speed of light and d is the layer thickness. ε_{Sub}, ε_{Air} and ε_{ITO} are the dielectric constants of the glass coverslip, the surrounding air and the ITO layer respectively. Linden et. al [21] reported a cut-off energy of 0.73 eV (which corresponds to a wavelength of 1700 nm) with the parameters d = 140 nm, $\varepsilon_{Sub} = 2.1$, $\varepsilon_{Air} = 1$ and $\varepsilon_{ITO} = 3.8$.

Normally, guided modes cannot be excited in a slab waveguide by light with an incident angle normal to the plane; the incident light must approach at an angle which allows total internal refraction and the propagation of the light wave through the waveguide. However, the metal nanoparticles situated on the surface acts as a grating coupler, diffracting the beam into the waveguide. The phase matching condition of a one-dimensional grating coupling is [29]

$$\boldsymbol{\beta} = \boldsymbol{k}\, sin\theta \pm i\boldsymbol{g} \qquad (2.33)$$

where **β** is the propagation vector, **k** is the incident wave vector and $i\boldsymbol{g} = \frac{2\pi}{a}$ where a is the distance between the gratings and i = [1,2,3…] This can be applied to the regular array of particles present in the samples created (see section 5.1) in two dimensions using the following relation [21]

$$\boldsymbol{k}_{wg} = \boldsymbol{k}_{||} \pm i\boldsymbol{g}_x \pm j\boldsymbol{g}_y \qquad (2.34)$$

where $\mathbf{k}_{wg}$ is the wave vector of the coupled waveguide mode, $\mathbf{k}_{||}$ component of the incident light wave vector that is parallel with the x-y plane, and $i\mathbf{g}_x$ and $j\mathbf{g}_y$ are the reciprocal lattice vectors of the particle array, given by 2π divided by the distance between the particles in the x and y directions, respectively. The factors i and j are integers [1,2,3…] similar to equation 2.33. The optical measurement methods employed uses incident light normal to the sample surface, and as such the $\mathbf{k}_{||}$ term is zero. Consequently, the coupled waveguide mode is dependent only on the interparticle distances in the x and y directions. When coupled into the waveguide, the waveguide mode can take on one of two configurations: Transverse magnetic (TM) or transverse electric (TE). The TE mode also has a larger photon energy for the same value of $\mathbf{k}_{wg}$, as illustrated in the dispersion relation of Figure 2.5.

These configurations are dependent on the incident light polarisation (see Figure 2.4). The waveguide modes coupled into the ITO film is phase shifted 180° relative to the particle plasmon, and when the spectral positions of the waveguide mode overlaps with the LSPR, the coupled light and the plasmon interact by destructive interference, resulting in a suppression of the LSPR extinction [21]. At energies close to the cut-off frequency, the waveguide modes mostly extend into the substrate, and as such are mostly given by the quartz light line (see Figure 2.5). However when increasing the photon energy, the modes are more and more confined to the ITO layer, and as such become ITO-like [21]. Therefore, the samples with longer

interparticle distances (corresponding to a smaller $\mathbf{k}_{wg}$ by eq. (2.34)) are expected to exhibit waveguide modes close to the quartz light line, while samples with smaller interparticle distances should have more ITO-like energies. Without the presence of the nanoparticles, the light would couple into to degenerate waveguide modes propagating in opposite directions, resulting in a single supressed dip in the extinction peak. However, as shown by the measurements in section 5.4, there are two dips instead of one. This was attributed by Linden et. al [21] to the Bragg scattering of the waveguide modes by the particle array, which leads to the formation of standing waves under and in between the particles. These standing waves have a different dielectric environment, which removes the degeneracy. In addition, if the waveguide modes appear outside of the plasmon, it is expected to appear as an extinction peak due to lack of destructive interference with the particle LSPR.

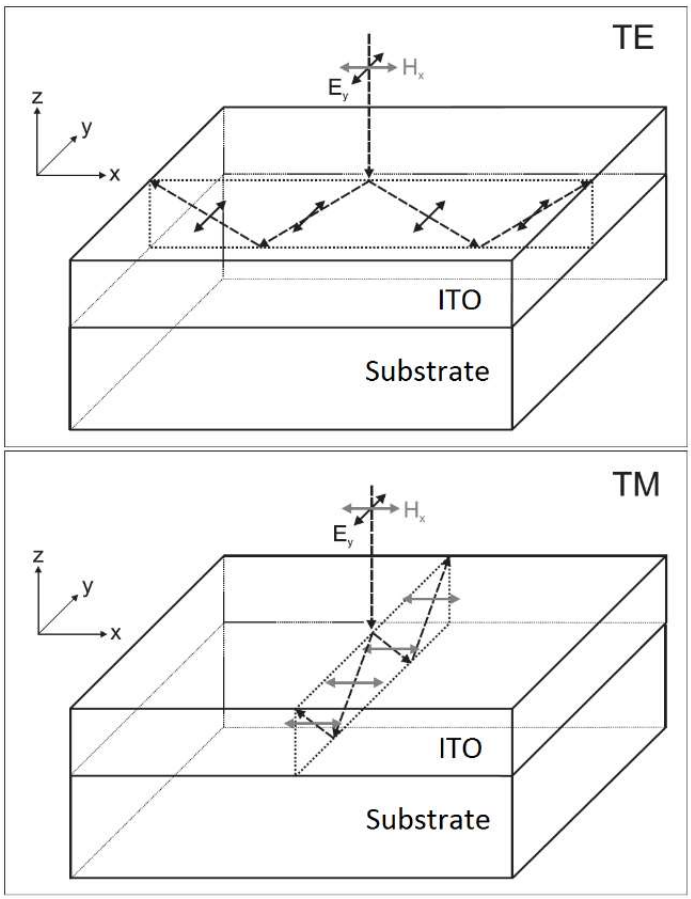

Figure 2.4 Illustration of transverse electric (TE) and transverse magnetic (TM) waveguide modes. The propagation direction of the waveguide mode is the deciding factor of whether the particles in the x or y-directions are affected. Figure taken from [21].

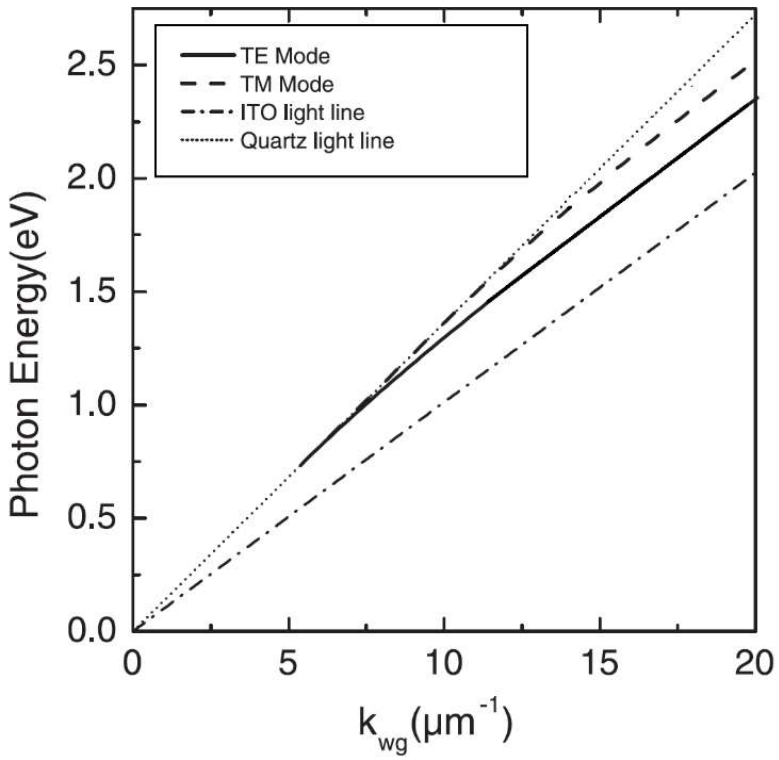

Figure 2.5 Dispersion relation of the TE and TM waveguide modes. Note that k_{wg} is entirely dependent on the interparticle distances as shown in equation 2.34, while the spectral positions of the suppression dips would be found on the photon energy axis. Figure taken from [21].

3 Experimental Equipment

3.1 The Nanotechnology Laboratory at UiB

UiB's nanolab consists of four different sections with varying degree of air purity. The purity is measured according to how many particles of sizes above 0.1μm are present per cubic meter, and is represented by the ISO standard where ISO 9 corresponds to outdoor air [36]. The lower the number, the lower the concentration of particles, and the two cleanrooms uphold the ISO 5 and 7 standards. The two remaining rooms are a semi-cleanroom and a storage room. The air is maintained by a filtered air flow from the ceiling of the room. This creates a pressure gradient, which push out the excess air through slits in the wall at floor level, creating a continuous air flow. There are also restrictions on what you are allowed to wear inside the cleanrooms; All personnel must wear a lab coat, hairnet, a facial mask, and rubber gloves in order to prevent the introduction of additional particles. The highest-level cleanroom, ISO 5, contains a fume hood used primarily for spin coating and developing, as well as a thin film analyser and a reactive-ion etcher. The combined electron beam lithography and SEM-microscope is located in the ISO 7 clean room, and the semi-clean room contains a second fume hood and the electron beam evaporator used to deposit thin metal layers on the samples.

3.2 Electron Beam Lithography (EBL)

Electron beam lithography is a method of producing nanostructures that utilizes an electron beam to alter the chemical composition of a thin film deposited on a substrate. After the exposure, the film can be selectively removed using a developer, which is a solvent that dissolves either exposed, or un-exposed areas. If the exposed resist is dissolved by the developer, the resist is classified as positive, and conversely if only the exposed areas remain after development, the resist is negative. In this work, the resist used is called PMMA (poly-methyl methacrylate) which is a positive resist consisting of long chains of polymers. These chains are broken when exposed to the electron beam, making the resist more soluble. Subjecting the sample to the developer after exposure will only remove the exposed area, while the surrounding resist stays intact [37].

While this method provides great reproducibility and resolution down to the sub-10 nm regime [38], it is also very time consuming, given the fact that the electron beam has to write each structure by passing the beam across the resist surface. In contrast to optical photo-lithography, where you can illuminate large areas at once and use a mask to create your patterns, this is not possible when dealing with nanoscale structures as the resolution of the mask pattern is limited by diffraction.

3.2.1 The Raith E-Line EBL-system

The system used to perform electron beam lithography in the UiB nanostructure laboratory is a modified scanning electron microscope depicted in Figure 3.1. The microscope has been outfitted with a beam blanker, a high precision laser interferometer to control the sample stage, and a pattern generator. These components enable a controlled and precise exposure of resist layers using a focused electron beam. The electrons are emitted from an electron gun situated in the top section of the electron column, and accelerated through the column with the desired acceleration voltage. This system has a maximum acceleration voltage of 30 kV. Once accelerated, the beam is further controlled using an aperture, which essentially is a hole with varying diameter (7.5-120 μm) depending on the desired beam current.

The beam is then focused using electromagnetic lenses, and its position on the sample surface is controlled by deflection using magnetic coils. These scanning coils also double as a beam blanker, enabling the beam to quickly be deflected away from the sample altogether, as opposed to using a physical beam blanker which would require more time to close. Once the electrons hit the sample surface they interact in several different ways as detailed in section 3.3, and by collecting and measuring the energy of these electrons a picture can be created. The scattered electrons are collected using two detectors; The InLens detector, as the name suggests, is placed inside the lens directly above the sample, and collects secondary electrons emitted from the sample.

The secondary detector (SE2) is placed at an angle compared to the sample surface, and is equipped with a positive bias. This bias enables the collection of low energy secondary electrons created by interactions between the backscattered electrons and the chamber walls. The angled position of the SE2 detector also enables the detector to differentiate topographical changes in the sample. To create an image, the focused electron beam is scanned across the sample surface, and the electrons emitted from the sample are continually measured by the

detectors. One measurement corresponds to a pixel in the image, and its brightness is determined by the electron energy. The picture is formed by combining the position of the deflected beam and the measured energy to create each pixel. The amount of time spent measuring each point also affects the total electron "dose" delivered to the sample surface, which is crucial to control when writing nanostructures; If the dose is too high, a larger area per point will be exposed, resulting in a lower resolution pattern. The dose corresponds to the number of electrons interacting with your sample at a single point, and can be calculated using the beam current, dwell time and step size as shown in the equation below [39].

$$Area\ dose\ [\mu C/cm^2] = \frac{Dwell\ time\ [ms] \times Beam\ current\ [nA]}{Step\ size^2\ [cm^2]} \qquad (3.1)$$

The beam current is determined by the aperture and acceleration voltage used, as well as the state of the filament in the electron gun. Dwell time is the time spent on each point on the surface, while the step size is the length between each point. The dose is chosen based on a dose matrix (described in section 4.2). Once the dwell time has been calculated, the system is ready to write the sample design. The design is a CAD file containing all the exposure points, and can be created using the Raith E-line software or by importing any ASCII-file. Once the design is in place, the beam is deflected by the scanning coils to hit each point.

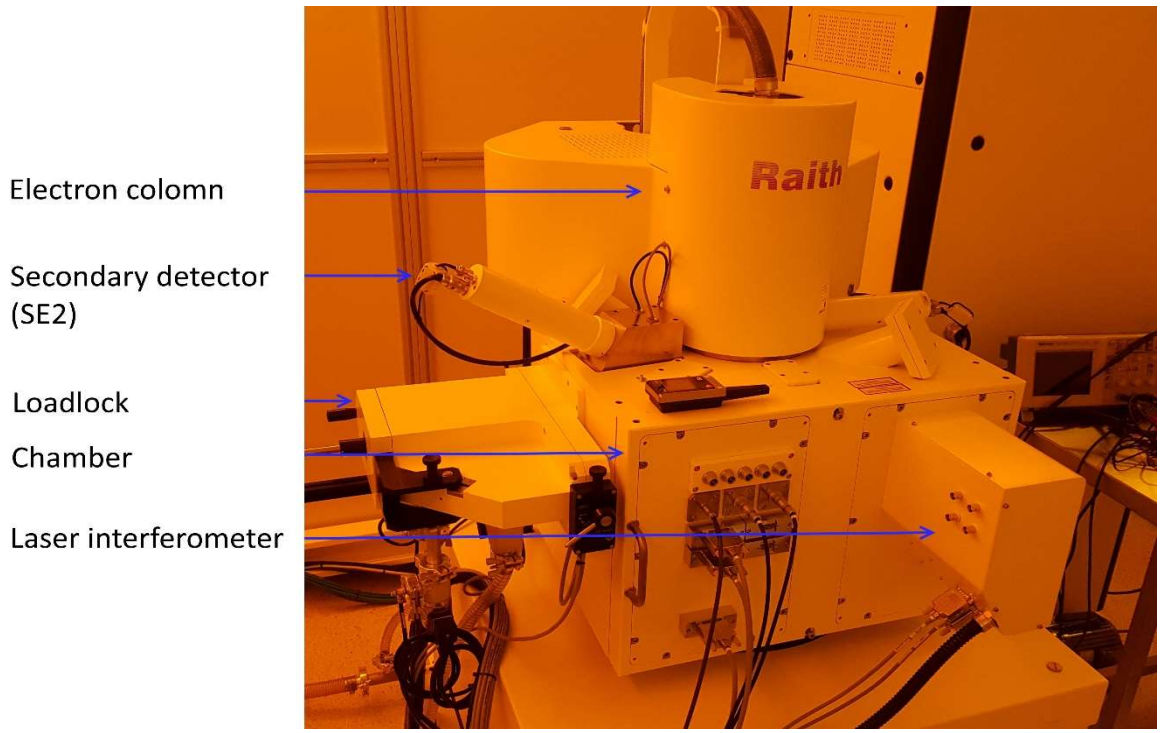

Figure 3.1 The Raith E-line electron beam lithography system.

However, as the deflection angle increases to reach the outer points of the design, the interactions between the resist and electron beam changes due to a non-normal beam incidence [39]. To alleviate this problem, the stage is physically moved for each 100 μm (one square of 100 x 100 μm is called a writefield). By moving the stage after the completion of each writefield, the sample can be stitched together.

3.3 Electron beam and resist interactions

The incident electrons that were accelerated through the electron column are called primary electrons. Once they hit the sample surface, they start losing their energy through inelastic scattering or collisions with other electrons. This scattering is called forward scattering. The scattering angle can also exceed 90 degrees, causing the electron to either continue laterally through the resist layer or exit the resist in the opposite direction from which it came. These are called backscattered electrons. When colliding with other electrons, some of the primary electrons energy is transferred which accelerates the electron with which it collided. These electrons are called secondary electrons, and they have the ability to both break the chemical bonds in the resist, and to create more secondary electrons themselves. Once enough collisions have taken place, the electrons no longer have enough energy to break the bonds in the resist, at which point they will no longer affect the resolution. Therefore, even with a perfectly focused electron beam down to a few nm, the actual resolution is limited by this cascade of secondary electrons [40].

3.3.1 The resist

The resist used in this work is called PMMA (Poly(methyl methacrylate)) which consists of long chains of polymers. It is a positive resist, meaning once its chemical bonds are broken by the electron beam it becomes more soluble, and the exposed areas dissolves when subjected to a developer. Two different resist schemes are employed in this thesis, as illustrated in Figure 3.2. The resist walls are tilted inward towards the substrate, which is a product of the secondary electron cascade effect. This is a desirable shape, because it ensures that the resist walls are not in contact with the metal particles when they are deposited on the substrate surface, which makes it easier to successfully perform the lift-of procedure. In the bi-layer scheme, the bottom layer is a more sensitive resist, which decreases the angle between substrate and resist even

further. The resist sensitivity is a function of the binding energy between the polymer chains; a low binding energy makes a high sensitivity resist that required less electron exposure to break the chemical bonds.

Figure 3.2 Illustration of resist schemes. The left figure shows a single layer resist, while the right shows a bi-layer resist.

3.3.2 Substrate

The substrate used in this work is a ITO (Indium tin oxide) covered borosilicate glass coverslip, manufactured by Diamond Coatings, UK. The ITO-layer is 300 ± 20 nm thick, and is electrically conducting which is a useful property when imaging and performing EBL due to the lack of charge build-up on the sample surface. The substrate also has above 80% transparency in the visible wavelength range [41], making it ideal for extinction measurements.

3.4 The Filmetrics Thin Film Analyser

The Filmetrics F10-RT thin film analyser is located in the ISO 5 cleanroom at the laboratory, and uses a tungsten halogen light source with a spectrum of 380-2000 nm to illuminate the sample. The reflected and transmitted light is then collected directly above and below the sample stage, giving rise to a reflection- and transmittance spectrum respectively. In this work, the transmittance spectrum is used to obtain the extinction of the MNPs, and both the reflected and transmitted spectra are used to determine the thickness of the spin-coated PMMA resist layers of all the samples. The spectrometer measuring the spectrum has a range of 380-1050 nm. When calculating the thickness of the resist layers, the results are displayed as a measured thickness, as well as a "goodness of fit" value. This is a number between 0 and 1, and represents the agreement between the measured and theoretical spectrums. In other words, a goodness of fit value of 1 corresponds to a perfect match between the measured and the calculated spectra.

Figure 3.3 The Filmetrics thin film analyser

3.5 Electron beam evaporator

The Temescal FC 2000 electron beam evaporator is used to deposit thin metal films evenly on the substrates surface. The principle of electron beam physical vapour deposition is to heat up a metal to the point of evaporation using an electron beam pointed towards a crucible containing the metal. The electron beam is accelerated by a 10 kV voltage and guided towards the crucible using a magnetic field. Once the metal has been heated to the point where you have a steady flow of gaseous metal atoms, the sample is exposed and coated by precipitation of the metal. The metal atom flow rate is calculated using a quartz crystal that changes its resonance frequency when the metal is deposited on its surface.

Once the desired rate is achieved, the sample is exposed for the amount of time required to obtain the desired metal layer thickness. This process takes place in a low pressure (1.5 x 10^{-6} bar) to ensure free passage for the electrons to reach the crucible, lowering of the sublimation temperature of the metal, and reducing surface contamination inside the chamber.

Figure 3.4 The Temescal FC-2000 electron beam evaporator. The sample is inserted into the process chamber via the dome on top of the machine.

3.6 Transmission spectrometer

The transmission spectrometer (TS, depicted in Figure 3.5) was newly installed in the UiB nanolab and is used for the first time for systematic experimentation in this thesis work. It consists of a tungsten halogen light source (Ocean Optics HL 2000) with a wavelength range of 360-2400 nm. The light is directed through a convex lens (Thorlabs LB1901-A) by a fibre optic cable, and subsequently reflected up through the sample stage by a mirror. The beam spot size is approximately 0.5 mm. The sample stage can be moved using micrometre screws. Between the mirror and the sample stage an adjustable calcite polarisation filter (Thorlabs GTH10M) is employed to control the beam polarisation. Once the beam has passed through the sample stage, it passes through a 4x magnification objective (Thorlabs RMS4X) and is subsequently split 50/50 up to a camera on top of the system (Thorlabs DCC1545M) and a fibre optic cable leading to the detector (Ocean Optics USB4000). The detector is controlled by the SpectraSuite software and the camera by the ThorCam software. The theory behind

transmission spectroscopy is presented in section 2.5, and the measurement procedure is described in section 5.4.

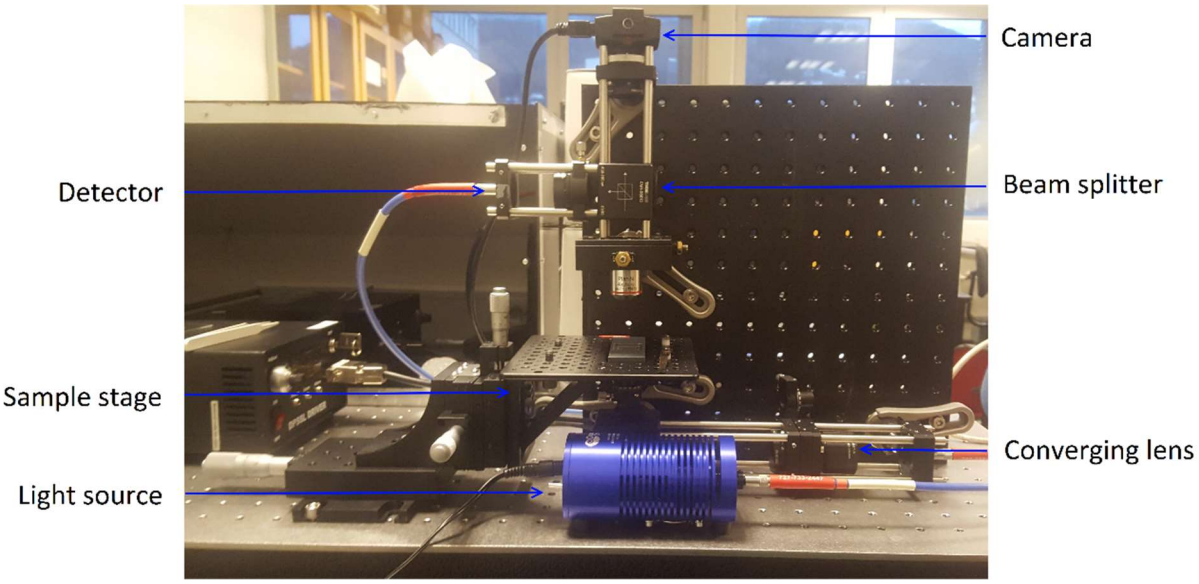

Figure 3.5 The Transmission Spectrometer.

4 Sample preparation

In this chapter, preparation of the samples used for the work presented in this thesis is described in detail. The samples prepared are large 1x1 mm arrays of 150 nm gold nanoparticles, with interparticle distance varying between 350 and 450 nm. These arrays are placed on glass coverslips coated with ITO (Indium tin oxide). The production steps employed follows the method used by Håvardstun [42] *and Flatabø* [43]*, however, some unforeseen issues related to particle adhesion to the substrate surface occurred, which made it necessary to make some modifications. The production steps are therefore described chronologically with the iterative process of employing changes to improve the quality of the samples.*

4.1 Production of nanoparticles using EBL

This section describes the step-by-step procedure of nanoparticle fabrication. It is presented in chronological order, and highlights the reason why each step is important to the quality of the resulting particles. The overall aim is to create large 1x1 mm arrays of nanoparticles suitable for testing in a transmission spectroscopy setup. This is a large and time-consuming sample by EBL standards and each sample contains between 5 and 7 billion particles, however these dimensions are necessary to obtain good optical measurements. The desired particle geometry is 150 nm in diameter discs with a height of 20 nm (see section 5.1), and an distance between them corresponding to at least 2.5 times the particle diameter in order to avoid near-field coupling between the localised surface plasmon excitations [44].

4.1.1 Resist spin-coating

The first step of the electron beam lithography production is to coat the substrate with a lithographic resist. Prior to spin-coating, the ITO coverslips and all the equipment such as tweezers, pipettes etc. were rinsed using three different solvents in the following order, to remove contaminations from the surface:

1. Acetone (Emparta ACS, Merk KGaA)
2. Methanol (Emparta ACS, Merk KGaA)
3. 2-Propanol (Emparta ACS, Merk KGaA)

After rinsing, both substrate and equipment were blown dry using nitrogen gas. Once clean, the substrate was fastened to the spin coater (Chemat Scientific, KW-4A) using a sticky pad situated on a metal disc, which in turn connected to the rotor using a vacuum pump (see Figure 4.1). Two different resist schemes were employed in this work:

Single layer: PMMA 950K (Allresist AR-P 672.08) diluted in Anisole with a ratio of 2:3

Bi-layer: PMMA 495K (Microchem 495K PMMA A8) diluted in Anisole with a ratio of 2:3 as the bottom resist layer, and PMMA 950K (Allresist AR-P 672.02) on top.

The resists were deposited on the substrate surface using a pipette, and the substrate was spun around its own axis to distribute the resist layer evenly across the surface with the desired thickness. The thickness of the resist layer is determined by the rotation speed. To ensure an even distribution, the spin-coating takes place in two steps. First, the substrate was rotated at 500 rpm for 6 seconds to even out the layer and get rid of most of the excess resist, and subsequently the rotation speed is sped up to the desired spin speed for 60 seconds. Once the resist was distributed, the sample was placed on a hotplate (UniTemp GmbH – Eurotherm 2132) with a temperature of 175 °C for several minutes to harden the resist layer and evaporate any residual PMMA.

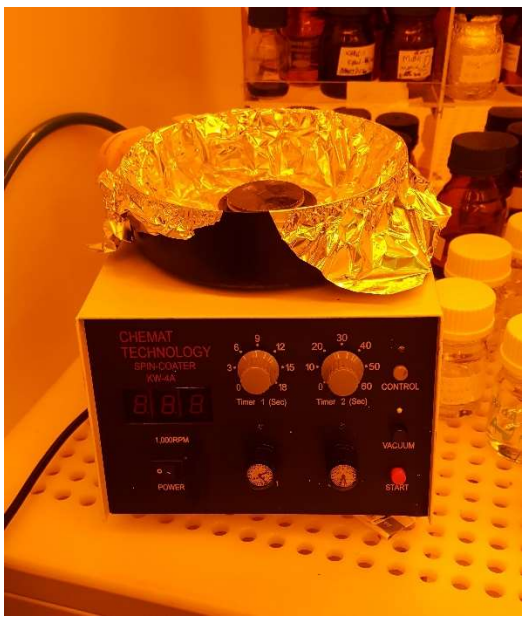

Figure 4.1 Chemat Scientific KW-4A Spin coater. When in use, the bowl is covered by a metal lid to prevent the resist from escaping.

The amount of time the sample was soft-baked depends on the resist scheme; in the single layer scheme the sample was soft-baked for 5 minutes, while in the bi-layer scheme the bottom layer of 495K resist was baked in 3 minutes and the top layer of 950K was baked in 6 minutes. The differences between a single and bi-layer resist scheme is detailed in section 3.3. In order to determine the spin speed corresponding to the correct resist thickness, several samples of silicon were coated with PMMA and subjected to different spin speeds. Silicon was used to determine this because of the transparent nature of both glass and the resist, which would otherwise be challenging to measure accurately. This resulted in samples with various resist thicknesses, describing the effect of different spin speeds on the thickness of the resist film, as shown below.

Using this information, one can calculate the speed required to obtain the desired thickness, which was 150-180 nm. This thickness is desirable for an easier lift-off and a more pronounced undercut profile, which is explained more in detail in section 3.3.1. Using the measurements shown in Figure 4.2 the spin speeds corresponding to the desired resist thickness was calculated. For the single layer, a spin speed of 4400 rpm led to a thickness of 175 ± 2 nm was obtained. For the Bi-layer resist schemes, the 495K resist required 5900 rpm to obtain a thickness of 80 ±1 nm, while the 950K resist had 4000 rpm corresponding to 69 ± 1 nm.

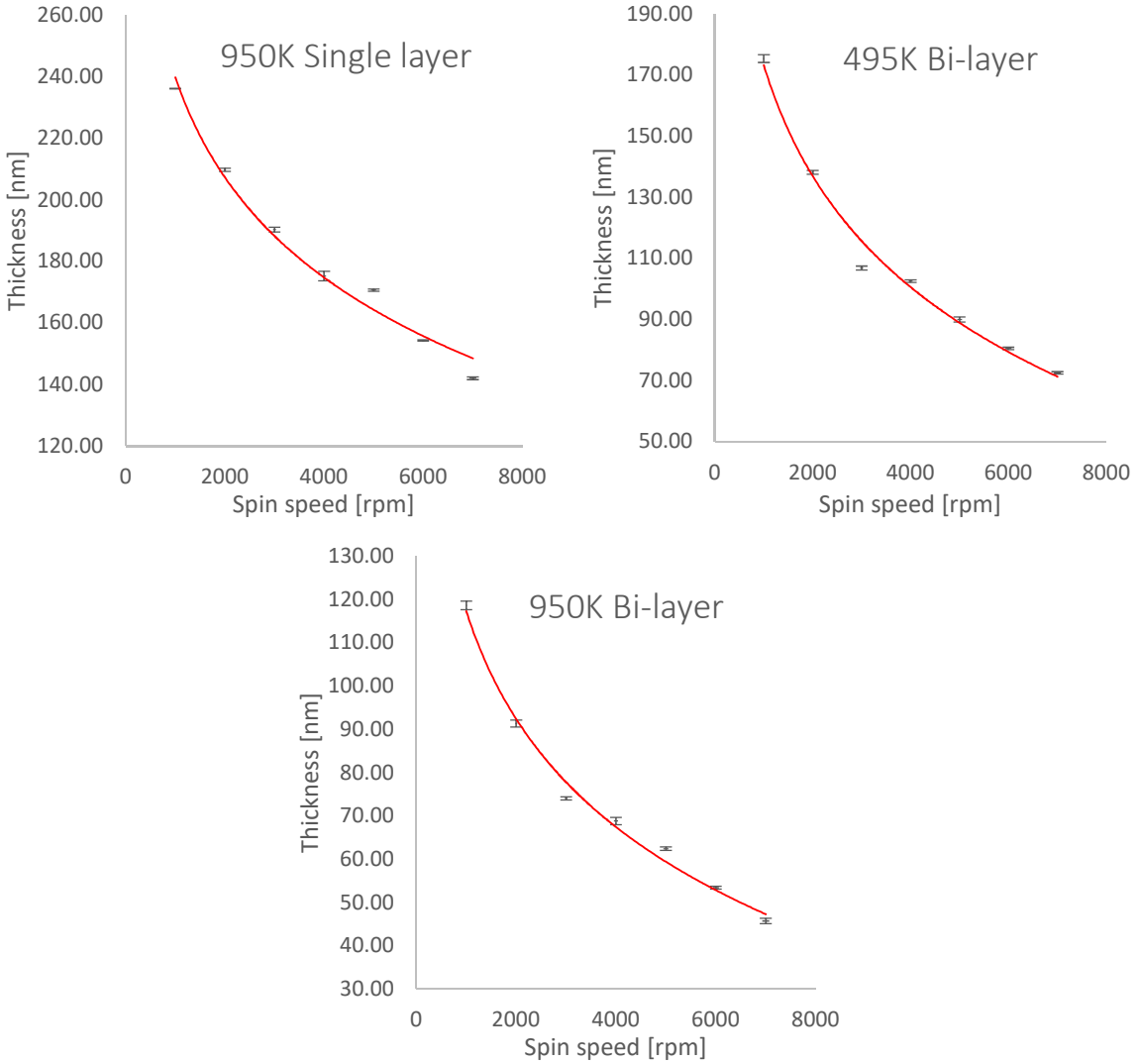

Figure 4.2 Resist thickness vs spin speeds. Measurements were taken using the Filmetrics thin film analyser. The vertical error bars are the standard deviation of three measurements at each spin speed, performed on different places on the samples, while the horizontal error bars accounts for the 1% error in spin speed from the spin-coater. This is the error described in the manual provided by the manufacturer of the spin-coater [45].

4.1.2 Electron beam resist exposure

Once the desired resist scheme had been deposited on the sample surface, it was ready to undergo electron beam exposure. The sample was placed in the sample holder of the Raith E-line SEM using a spring-loaded metal clip. After the sample was in place, small polystyrene beads were placed in one of the corners of the sample using a toothpick. The purpose of these beads is to be used as a focusing aid when calibrating the electron beam, as they are easily recognizable and have a distinct round shape. The sample was then loaded into the SEM using the loading procedure, and the desired electron acceleration voltage and aperture were chosen. In this work, all samples were produced using 10kV acceleration voltage and a 30 µm aperture.

When writing very small structures it can be beneficial to decrease the aperture size, as a smaller aperture increases the depth of field, at the cost of longer writing times due to a lower beam current. However, all the particles made in this work had a target diameter of 150 nm, so this was not necessary. After the voltage was turned on, the sample stage was moved to a height close to the electron beam focal point by mechanical movement, and then fine-tuned by adjusting the magnetic coils controlling the electron beam. In addition to focus, stigmation and aperture alignment was adjusted to get as clear an image of the beads as possible. Once a good image had been obtained, the writefield alignment procedure was performed on a distinctive feature on the sample surface that is recognisable at a low magnification, for instance a dust particle or a collection of the polystyrene beads.

This procedure calibrates the interferometer used to control the sample stage movement, and ensures high precision of stage movement between writefields (defined in section 3.2.1) which leads to minimal stitching errors. The writefield alignment is performed by depicting the chosen feature, and subsequently manually dragging vectors towards the feature from positions chosen by the computer. The computer then performs the same task automatically using the image contrast and brightness to determine the features position. Once this is determined accurately, the beam current is measured using a Faraday cup placed on the sample stage. This current is then used to calculate the dwell time between each step as described in section 3.2. Lastly, the desired pattern file is drawn or imported, and the beam exposure can start.

4.1.3 Chemical sample development

Development of the sample was done by lowering the sample into a beaker filled with the resist developer for 2 minutes. The developer used in this work was MIBK (AR 600-56):IPA with a ratio of 1:3. The resist used is positive, meaning that the areas exposed to the electron beam will be dissolved during development, leaving holes in the resist film. After development the reaction was stopped by rinsing the sample in 2-propanol, and blown dry using a nitrogen gun.

4.1.4 Electron beam physical vapor deposition

Once developed, the samples were placed in the electron beam evaporator (Temescal FC-2000), and a thin metal film was deposited on top of the resist. All samples were produced using 20 nm thick gold films, except for the dose matrices were 20 nm nickel was used due to its lower

cost. The samples were mounted on a circular disc using fastening clips, and the disc was installed in the process chamber. Once closed, the chamber vented into a high vacuum in order to match the pressure of the rest of the system, which always keeps a vacuum of 1.5 x 10^{-6} bar in order to prevent contamination. The desired metal and film thickness was then chosen in the Temescal software, and the metal film was then deposited on the sample surface, with the sample holder rotating slowly to ensure an even distribution. When deposition was completed, the system chamber was sealed off and atmospheric pressure was restored to the process chamber. Once the sample was removed the process chamber was vented once again to minimize contamination.

4.1.5 Lift-off procedure

The lift-off procedure removes the resist film, leaving the metal particles behind on the substrate. This was performed using a hotplate (Stuart CB160) and a petri dish filled with N-Methyl-2-pyrrolidone (NMP) on top of the hotplate. Temperature of the NMP was controlled using a thermometer that was lowered into the petri dish. Once the NMP stabilized at 80°C, the sample was lowered into the petri dish. Previous work by Flatabø [43] and Eidsvåg [17] reported an exposure time of about 10-15 minutes during single layer resist lift-off, in addition to cracking of the metal layer before it loosened. When performing the procedure, it took at least 15 minutes until the metal layer started to puff up, and at no point did the layer crack. After 30 minutes the layer detached from the sample.

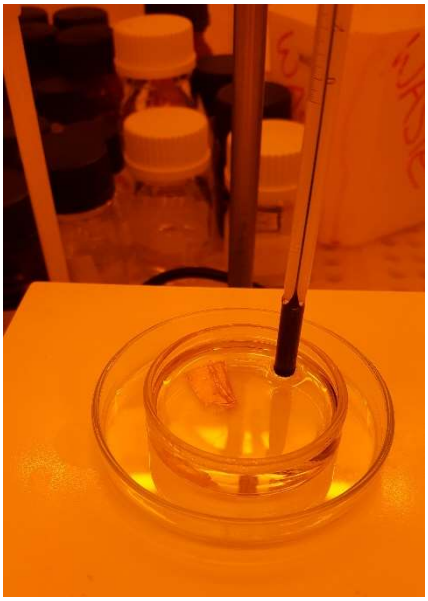

Figure 4.3 The lift-off setup

With the bi-layer resist scheme (described in section 3.3), Eidsvåg reported an increase to about 40 minutes for the layer to detach, which is consistent with this work. One possible reason as to why the single layer resist took longer to detach in this case is that the resist layer was thinner than intended. To investigate this, three samples of silicon wafer were spin-coated and measured as described in section 4.1.1. The resist layers were found to be 174 ± 1 nm, which is consistent with the desired thickness. Another possible reason could be contamination or aging of the NMP used, and a newly acquired bottle was opened and lift-off performed to

investigate this, showing no difference in exposure time. As such, the reason why this procedure took longer than previously reported is still unknown.

4.2 Dose matrices

When determining the correct writing parameters for the resist used, a dose matrix is made. The matrices consist of the same pattern repeated with different dosages, so that the best fit can be determined. The first dose matrix produced was a 3x3 grid of writefields with a side length of 100µm. Each writefield were exposed to a fraction of the standard dose, which was set to 100 µC/cm^3 based on the work of Håvardstun [42]. The particle size was set to 150 nm in diameter, with a 500 nm interparticle distance in both the x and y direction. All structures were written using a 10 kV acceleration voltage and a 30 µm aperture.

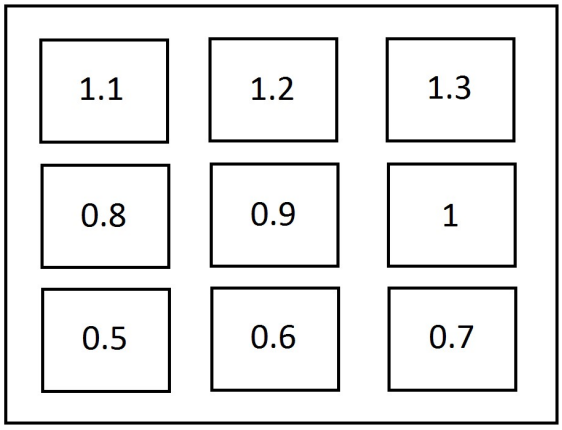

Figure 4.4 Illustration of writefield design, the number inside each square denoting the multiplication factor of the nominal dose.

In order to focus the electron beam in the sample surface, polystyrene beads were deposited in the corner of the sample using a toothpick. These beads are easily identifiable in the microscope, and has a circular shape which helps in adjusting the stigmatism of the electron beam. This focusing process is described in detail in section 4.1. After the sample was exposed by the electron beam and developed using the technique described in the previous section, the pattern was investigated in the SEM. This was done in order to confirm that the development process worked, and also to attempt to correlate the pattern in the resist to the resulting particle sizes. When investigating patterning directly on the PMMA it quickly became apparent that the electron beam damaged the resist layer in a matter of seconds, causing a blurring of the image. To minimize exposure while still measuring the correct positions, the measurements were

performed using a coordinate system; The stage was moved while the beam was blanked out, to the right spot using the coordinates. The electron beam was then unblanked to picture the sample with minimal exposure. Three pictures were taken at each measurement position at different magnifications, to measure both the diameter of the holes and the distance between them.

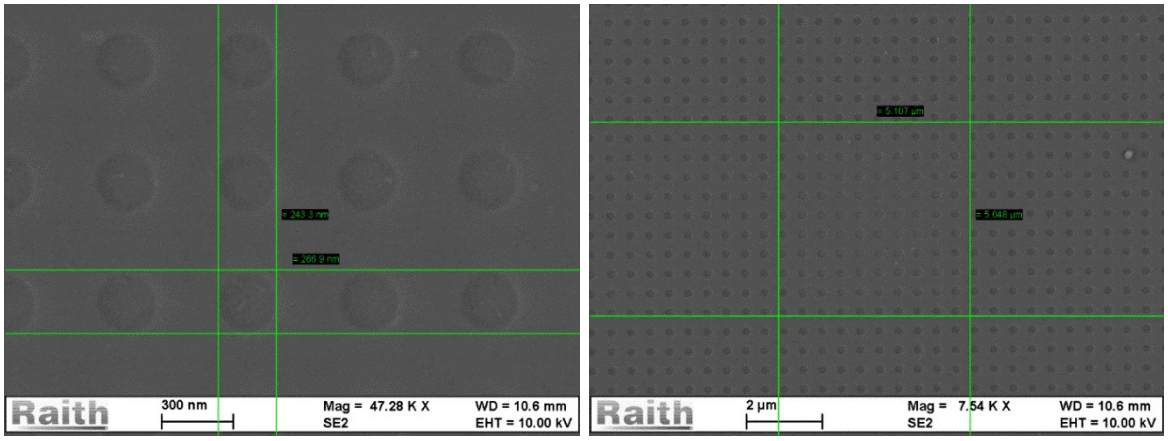

Figure 4.5 Holes in the PMMA resist film. This is the X=3 Y=2 writefield, corresponding to exactly the nominal dose of 100 µC/cm^3. Note that the diameter of the holes are larger than the design size of 150 nm, however the resulting particle diameter can only be determined accurately by measuring the actual particles. The right pane shows a zoomed out view used to measure interparticle distance. The distance was obtained using the average distance between 10 particles

The next step was to deposit a metal layer onto the PMMA surface, and subsequently remove the resist layer, leaving the particles behind on the substrate surface. The metal deposition and lift-off process is described more in detail in section 4.1.5. The first matrix did not however result in a sufficient number of particles; only trace amounts were found, including particles still attached to the metal layer.

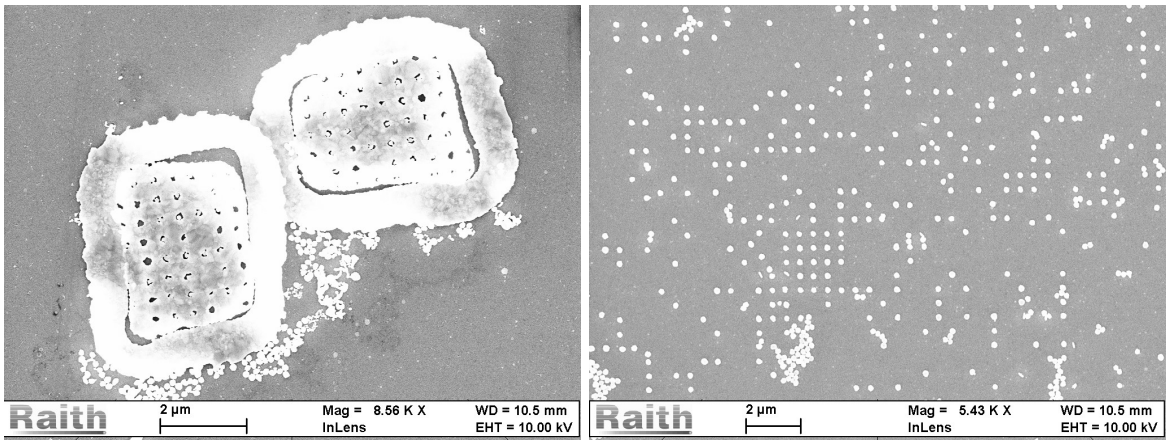

Figure 4.6 SEM-inspection of the 3x3 dose matrix after lift-off. Although some semblance of a particle grid can be seen in the right pane, there is not enough to make any legitimate measurements. The left pane depicts pieces of the gold metal layer, where some of the particles appear stuck in the holes of the layer.

The missing particles were at first attributed to an insufficient dosage, preventing the electron beam from reaching all the way through the resist. This would cause the particles to stick to the metal layer and subsequently be dragged off during lift-off. To test this theory, an extended 4x4 writefield dose matrix was created, enabling a larger variety of doses. The nominal dose was kept at 100 $\mu C/cm^3$, but the larger design allowed for a multiplication of the nominal dose ranging from 0.3 to 1.8. The design arrangement was equal to that presented in Figure 4.4, only with a 4x4 grid as opposed to 3x3.

This led to very similar results, with the pattern being visible once the areas exposed by the electron beam were removed during the development process. However, after lift-off the particles still did not stick sufficiently to the surface, indicating that the dose was not the problem. Another possible reason for the lack of particle adhesion could be contaminants on the ITO surface, and to investigate this the coverslips were sonicated for 10 minutes in each of the three cleaning solvents (Acetone, methanol and isopropanol) prior to spin-coating.

The coverslips were placed in a sample holder, and lowered into a beaker filled with cleaning solvent. The beaker was then placed into the water bath of the sonicator, which exposed the sample to sound waves of ultrasonic frequency of >20 kHz. The vibrations creates cavitation bubbles in the solvent, producing a kinetic motion of the fluid that enhances the cleaning process [46].

Figure 4.7 The sonicator setup. The sample holder could contain up to 6 coverslips at once.

Knowing that the dose was most likely not the cause of the missing particles, a size matrix was made instead of a dose matrix. The principle behind a size matrix is similar to that of a dose matrix, except the dose is kept constant while the size of the particle design is varied. In order to further verify that the dose did not contribute to the missing particles, three size matrices

were made with doses of 100, 110 and 120 µC/cm^3. Their design included one 100x100 µm writefield per particle diameter, with diameters ranging from 80 nm to 160 nm as illustrated below.

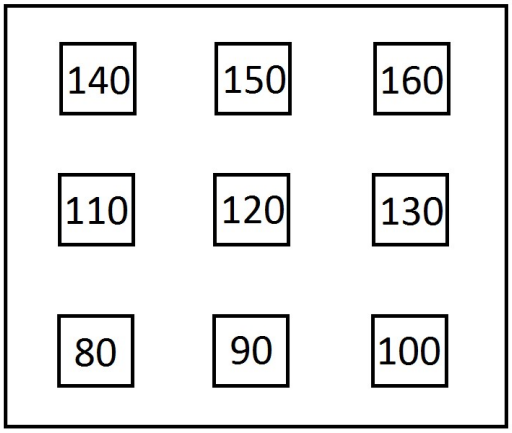

Figure 4.8 Size matrix design. The number indicates the particle diameter in the writefield, and the spacing between the writefields were 100 µm.

With this design and the sonicated substrates, the quality of the samples improved somewhat, however the particle adhesion was still not sufficient as shown in Figure 4.9.

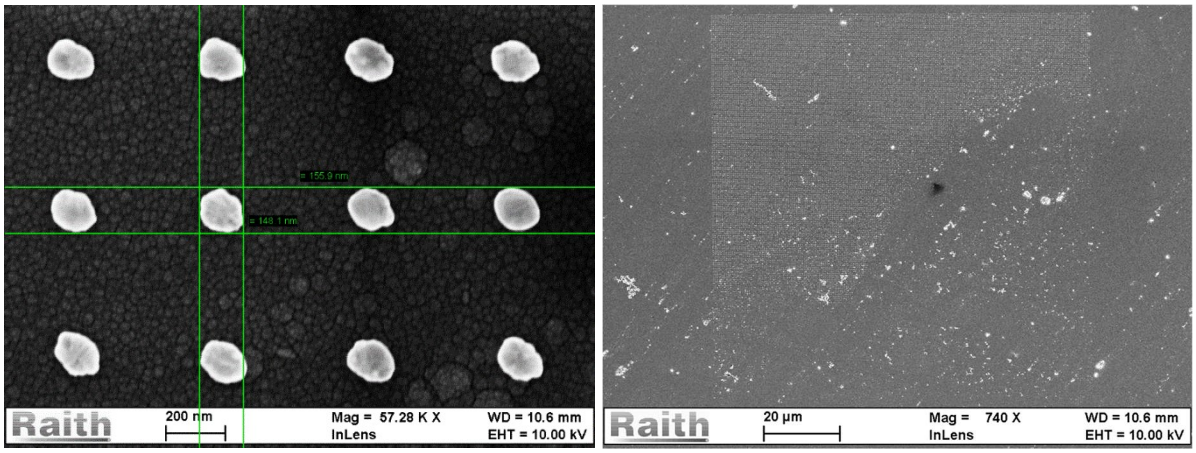

Figure 4.9 Size matrix after lift-off. These pictures show one of the writefields of the size matrix, with a nominal particle diameter of 150 nm and a nominal dose of 110 µC/cm^3. All the other particle diameters and dosages showed similar results. The intact particles on the surface were of fairly high quality, but the lack of particle adhesion did not encourage large scale sample production.

The fact that particle adhesion was poor across all nominal dosages and particle diameters indicated that nominal dosage did not contribute to the adhesion issues, and while the sonication of the substrate did indeed improve the quality of the sample it was still not good enough for large scale production. In order to further improve the quality, an attempt was made to improve

the focusing technique. In the previous samples, the electron beam was focused using polystyrene beads in the corner of the sample, and this might not result in an optimal focus at the writing area due if the sample is slightly tilted. To alleviate this, the beam was moved approximately half a millimetre outside the writing area, and refocused there. Since the sample was covered in non-conducting PMMA-resist, imaging proved to be somewhat challenging. Once focus had been obtained however, using for instance a dust particle or one of the clusters in the grain-like ITO structure, the quality of the focus could be inspected by utilizing the dot exposure function of the electron microscope. This exposes a single point for approximately 2 seconds, leaving a small mark in the resist film. The size and shape of this mark is an indication of the quality of the focus and stigmation respectively, where you want the dot to be circular and as small as possible.

Using this method, in combination with sonication of the substrate, particle adhesion improved, which allowed for accurate size measurements. The increased particle adhesion was attributed to an improved focus using the dot exposure technique. Adhesion improved for all dosages, 110µC/cm^3 were chosen as standard and employed on all consecutive samples. The particle diameters were found using a coordinate system based measurement scheme, where three different parts of the writefield was measured twice as exemplified in Figure 4.10.

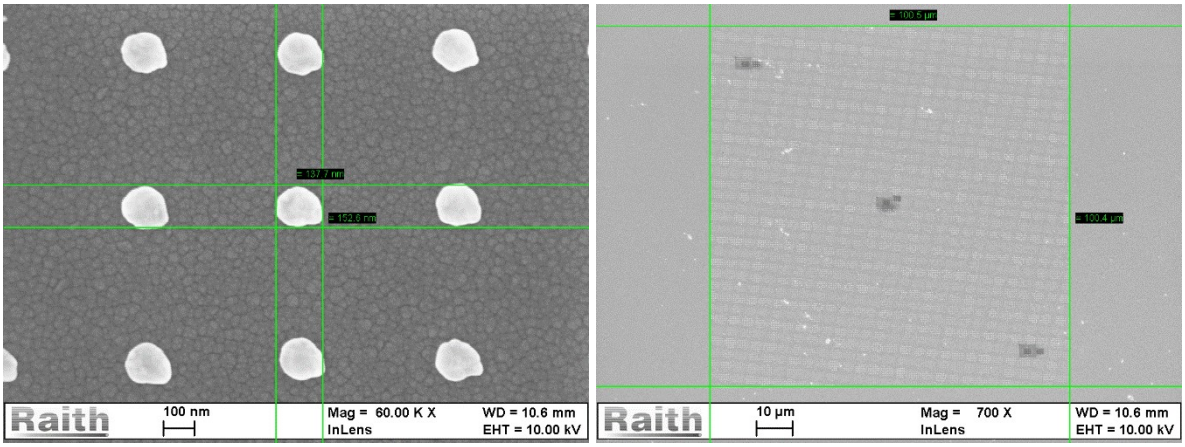

Figure 4.10 Picture of ITO size matrix used to calculate particle size. Both frames show particles with a circular design of 130 nm and a dose of 110µC/cm^3. Note the dark spots in the right pane, which shows the positions used to measure the particles. Two pictures like the one in the left pane were taken on each site. The small protrusions in the lower right corner of the particles, as discussed in section 5.2, can also be seen here.

The results of these measurements are shown in Figure 4.11. and shows a linear relationship between the measured and intended design size. Using a linear trendline and the corresponding linear formula, the design size corresponding to 150 nm in measured diameter was chosen as the particle diameter of the first sample, which was 105 nm.

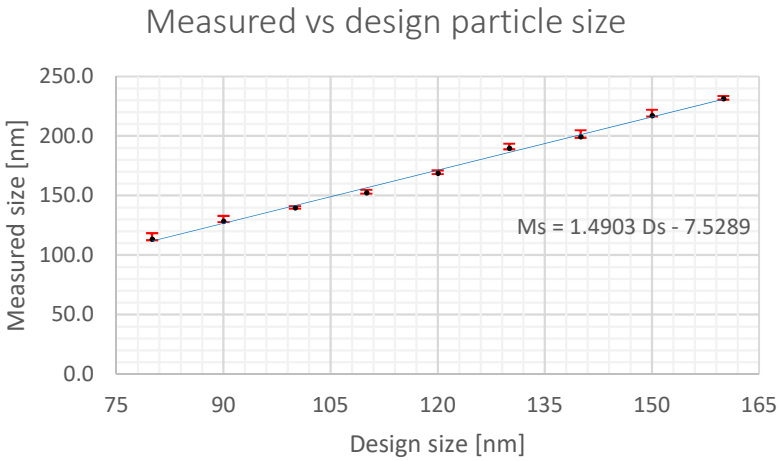

Figure 4.11 Size matrix particle diameter. This figure shows the measured particle diameter compared to the design size. The error used was standard deviation. Ms is measured size, Ds is design size.

4.3 Single layer samples

Two single layer samples were produced using the sonication and focusing techniques described above. The EBL writing parameters are shown in Table 4.1. The samples were designed to contain five 1x1 mm arrays on one 20x20 mm coverslip. The beam focusing was performed manually for each 1x1mm array in order to prevent loss of focus due to sample tilt. When investigating the sample in the SEM after production it became clear that particle adhesion was not sufficient across the larger 1x1 mm arrays as compared to the 100x100 µm dose matrices, as evident from Figure 4.13. Some of the samples were of sufficient quality, most notably SL_375 and SL_450, however due to the inconsistency of the results the production method was not deemed good enough.

It is possible that an error was made in one of the production steps, and therefore a second sample was made using the same parameters. The lift-off procedure took noticeably longer than that of previous works as discussed in section 4.1.5, and in an attempt to improve on the lift-off process a tilted sample holder was made. It is the heat transferred from the hotplate, along with the convections of the NMP liquid, that causes the metal flake to lift away

from the sample surface once the resist layer has been dissolved, and so the idea of the tilted plane was to have the metal flake roll of the sample with the help of gravity. It turned out however that the gravitational force on the metal layer is negligible, because as seen from the metal layer curled upwards.

Figure 4.12 Tilted sample holder used for lift-off

The second sample had very similar results, where most of the samples exhibited loose or missing particles. This lack of particle adhesion is surprising, given that the writing parameters used are based on the work of Håvardstun [42] who did not report any issues with missing particles. The particles are most likely loosened during the lift-off process, and the underlying reason could be a lack of an undercut profile as discussed in section 3.3.1. A potential solution to this is to employ a bi-layer resist scheme.

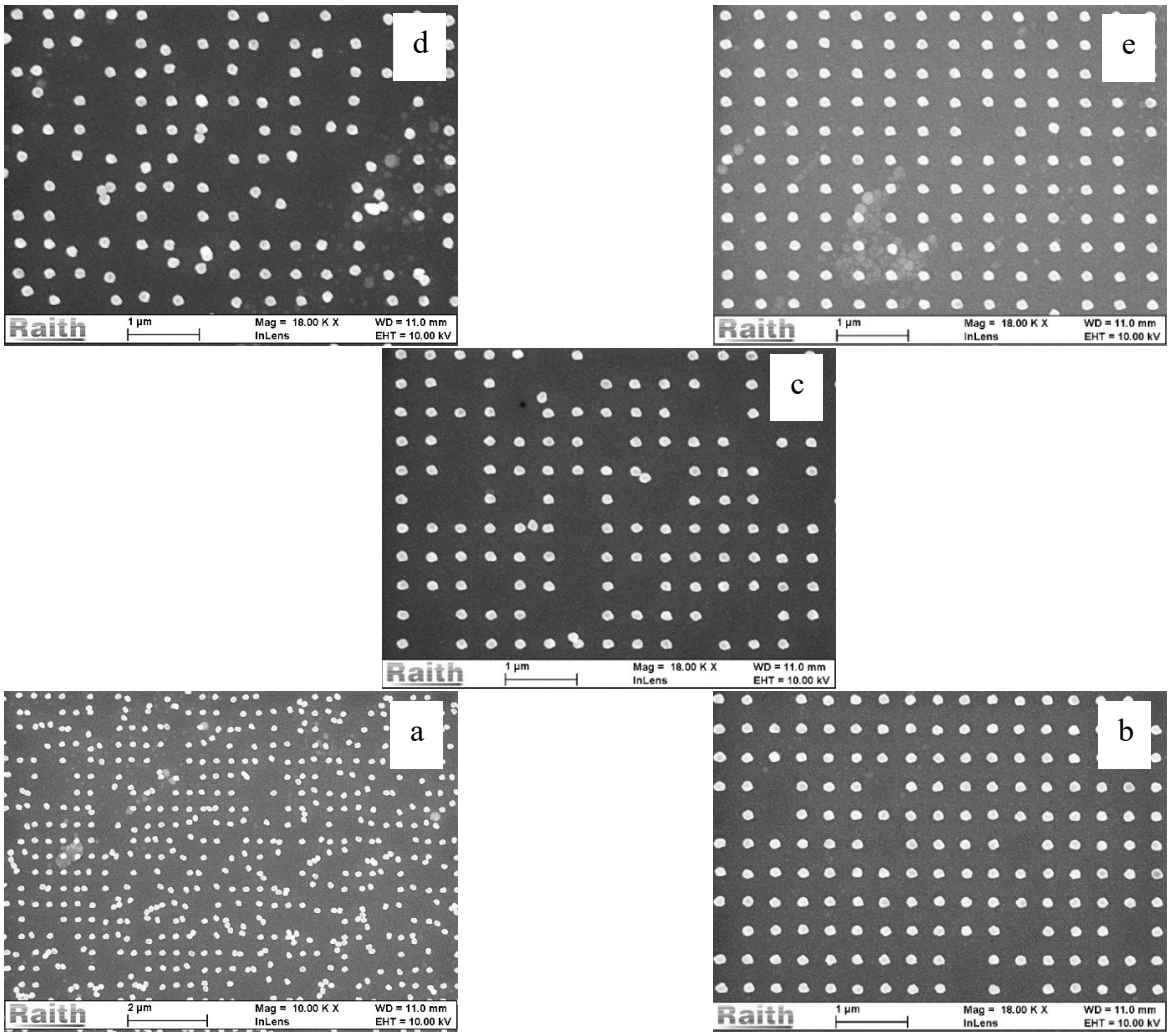

Figure 4.13 SEM images of single layer sample 1. The images are arranged in the same manner as the original design. Figure a denotes SL_350, b SL_375, c SL_400, d SL_425 and e SL_450.

Table 4.1 EBL writing parameters of single layer samples. The measured beam current did not change between the writing of the two samples.

	SL_350	SL_375	SL_400	SL_425	SL_450
Interparticle distance (x,y) [nm]	350,400	375,400	400,400	425,400	450,400
Nominal diameter [nm]	150	150	150	150	150
Design pattern particle diameter [nm]	105	105	105	105	105
Array area [mm^2]	1	1	1	1	1
Number of particles [x 10^6]	7.15	6.65	6.25	5.88	5.55
Aperture [µm]	30	30	30	30	30
Acceleration voltage [kV]	10	10	10	10	10
Measured beam current [nA]	0.195	0.195	0.195	0.195	0.195
Dose [µC/cm^3]	110	110	110	110	110
Writing time [min]	68	63	59.5	56.5	54

4.4 Bi-layer samples

Using the bi-layer resist scheme described in section 4.1.1, a new size matrix (with the same design as Figure 4.8) was made. This resulted in an immediate improvement in particle adhesion, which indicates that the reason for the missing particles in the single layer samples was indeed the lack of an undercut profile in the PMMA resist layer. The particle diameters were investigated using SEM, where 3 measurements were recorded from 5 different sites for each diameter. The results of these measurements are shown in Figure 4.14. These values were used to attempt to compensate for the larger particle sizes in the x-direction. The results of these samples are presented in chapter 5.

The writing parameters of the samples were chosen based on the work on bi-layer resists of Flatabø [43], which was confirmed to be working by producing dose matrices. All three samples were produced simultaneously, and the writing parameters are therefore equal.

Table 4.2 EBL writing parameters for bi-layer samples.

Acceleration voltage [kV]	Aperture [µm]	Measured beam current [nA]	Exposure dose [µC/cm^2]	Writing time [hours]
10	30	0.195	110	5

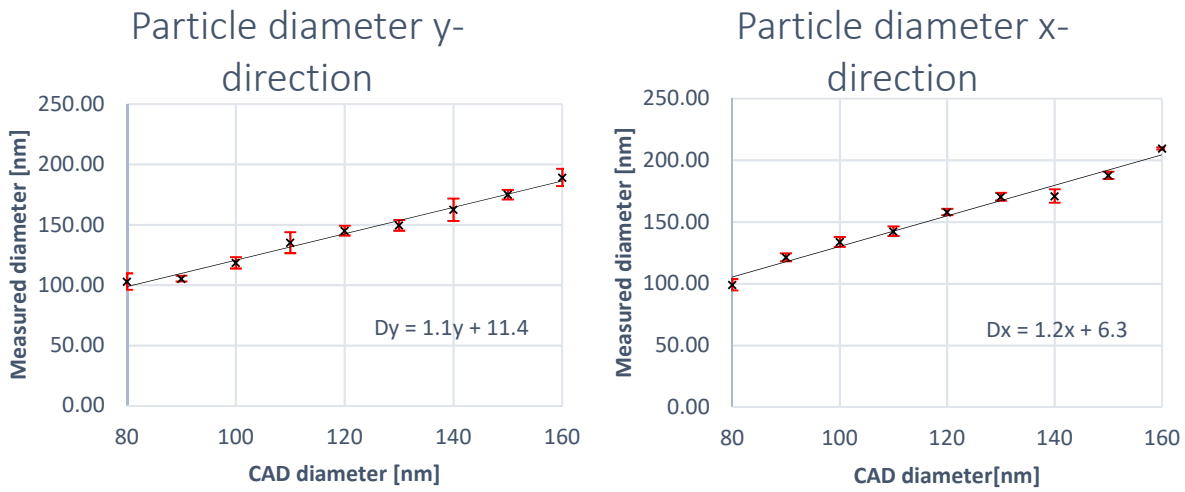

Figure 4.14 Measured diameters of bi-layer size matrix. Dy and Dx are the measured diameters, while y and x are the dimensions given in the design file. This corresponds to a design diameter of y = 126 and x = 120.

4.5 Summary – Sample preparation

The main problem encountered when manufacturing the particles were a lack of adhesion to the substrate, causing the particles to be dragged off during lift-off. Ultimately this problem was alleviated using a bi-layer resist scheme, which indicates that at least part of the reason why there was a lack of adhesion was because the particles got stuck to the rest of the metal layer, which is also depicted in Figure 4.6. The bi-layer resist provides more space between the resist layer and the particles (as explained in section 3.3.1) which evidently was sufficient to obtain three samples with a quality suitable for optical measurements.

5 Results and Discussion

Of the samples created, three were of sufficient quality to perform optical analysis. All samples were produced using EBL (described in section 3.2). The optical analysis was performed using the transmission spectroscopy setup and the thin film analyser described in section 3.4. The transmission spectroscopy measurement system includes a polarisation filter, which was used to isolate the effects of different polarisation directions. This was especially useful because of the asymmetrical nature of both the particles themselves and the differing interparticle distances depending on direction of the array.

5.1 Particle design

The sample names and design parameters are given in Table 5.1. These design values are based on the SEM-investigation of the combined dose- and size-matrices produced using the same EBL technique. All three samples were produced using the bi-layer resist scheme, which proved to be more effective during the optimization process (as described in section 4.1) compared to the single layer approach. The target dimensions of the particles were 150 nm in diameter, as this would give rise to a localized surface plasmon resonance in the spectral area coinciding with the extinction suppression of the interparticle distances (IPD) in the arrays [21]. This was also the reason why gold was chosen as the particle material.

Table 5.1 Design parameters of the samples. The sample name reflects the metal used to create the particles. All the samples were produced on an ITO substrate, with a particle height of 20 nm. The CAD diameter is the particle size in the design pattern.

Sample name	Target diameter (x,y) [nm]	CAD diameter (x,y) [nm]	Interparticle distance (x,y) [nm]
Au_IPD375	150,150	120, 126	375, 400
Au_IPD400	150,150	120, 126	400, 400
Au_IPD450	150,150	120, 126	450, 400

Each sample array consists of 10 x 10 writefields, which are squares with sides of 100µm, making each sample cover a square of 1 mm2. This was sufficient to perform accurate measurements, as the light spot from the spectroscopy setup is approximately 0.7mm. This was

determined by moving the sample on a stage controlled by micrometre screws, and moving the sample across the light spot. The transmittance spectrum was constant across the substrate surface, and changed notably when hitting the particle array. Therefore, by measuring the point just before the light hit the particles on both sides of the sample (1.7mm) and subtracting the sample width you find the approximate spot size.

At an interparticle distance of 2.5 times the diameter, the near-field coupling between plasmons can be considered negligible [44]. This means that the resulting plasmonic extinction can be compared to that of a single particle with regards to spectral position. It should however be noted that because of the selective suppression of the plasmon resonance caused by the repeating array, the plasmon position itself is hard to evaluate accurately. Furthermore, due to the different interparticle distances, the total number of particles will also differ slightly, with Au_IPD375 having a total number of ≈6.6 million particles, while Au_IPD450 has ≈ 5.5 million. It is therefore expected that the samples with smaller interparticle distance will have slightly higher extinction values.

5.2 SEM-characterization

In order to determine the shape and size of the nanoparticles, the samples were examined using SEM imaging. The particle arrangements, including interparticle distance, degree of missing particles, stitching errors and other defects were also investigated. All pictures were taken using a 10kV electron acceleration voltage, with a 30 μm aperture. The ITO layer on top of the quartz substrate is electrically conductive, which is a good imaging property because of the lack of charge accumulation on the surface. An insulating sample could otherwise cause the particles to appear smaller due to the changes in the scattering of the electron beam, caused by the accumulation of electrons on the surface [47]. The particle measurements were performed on 5 different sites of each sample, with three measurements of particle diameter, and one measurement of interparticle distance taken at each site.

The sites were located in each of the corners of the sample, and one in the middle in order to get a good representation of the whole array. Interparticle distances were averaged by measuring the distance between 10 particles. The results are presented in Table 5.2, with standard deviation used as error bars.

Table 5.2 Particle geometry. Note the difference in dimensions between x and y-directions.

Sample	Diameter x [nm]	Diameter y [nm]	Target diameter xy [nm]
Au_IPD375	160 ± 5	141 ± 5	150
Au_IPD400	158 ± 5	148 ± 3	150
Au_IPD450	150 ± 4	139 ± 4	150

Sample	Int. particle dist. x [nm]	Int. particle dist. y [nm]	Target IPD x [nm]	Target IPD y [nm]
Au_IPD375	376 ± 1	405 ± 1	375	400
Au_IPD400	405 ± 1	404 ± 1	400	400
Au_IPD450	455 ± 2	404 ± 1	450	400

As seen from the table, the particles are slightly elliptical in shape. An elliptical design, as opposed to a circular one, was chosen to avoid the elongation of the particles in the x-direction as described in section 4. This reduced the effect somewhat, but the particles still became larger in the x-direction. A larger particle size corresponds to a red-shift of the plasmon resonance, and such a shift is therefore expected when the incident light is polarised in the x-direction. The interparticle distance however remains quite consistent with significantly less variations.

The large differences in consistency between the particle diameter and the interparticle distances can possibly be explained by the method of writing; the particles were made using the area writing mode of the e-line EBL-microscope. This means that the electron beam will move in patterns to fill the area of the particles, presumably in a spiral motion. Because of this, the beam would need an exit point once the particle area has been exposed, which could be the reason why the particles are not perfectly circular, and that many of them have a small protrusion on the bottom left side, where the beam exits. These exit points are more visible on smaller particles, as shown in section 4.1. The alternative production method would be dot exposure, where the electron beam stays in one spot until the desired dose is achieved. The area mode was chosen because of the large particle size.

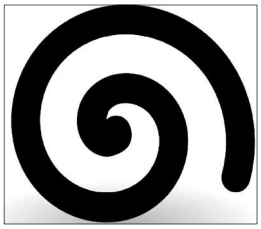

Figure 5.1 Illustration of presumed particle writing method.

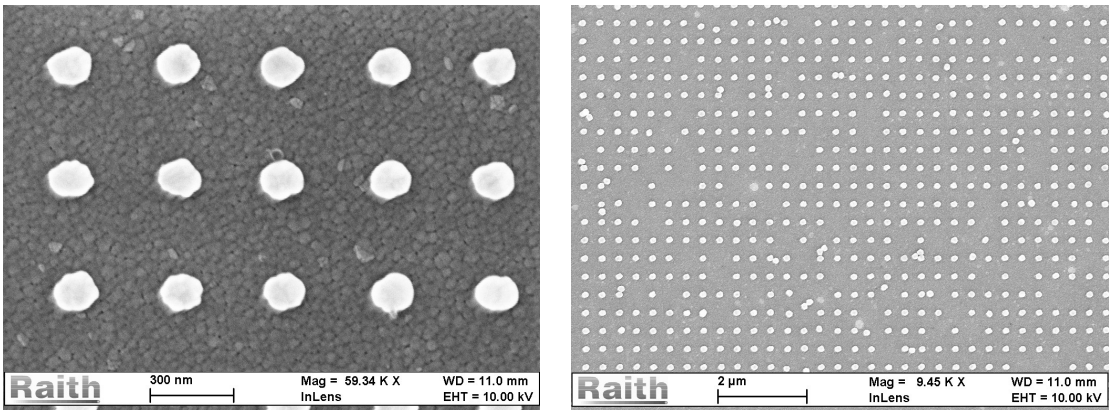

Figure 5.2 SEM images of Au_IPD375. The left image shows a close-up used to determine the diameter of the particles. The grain-like structures beneath the particles is the ITO-layer. The right image shows an overview of the sample, giving an indication of the degree of missing particles and consistency of the array. The particle diameters of Au_IPD375 was found to be 160 ± 5 and 141 ± 5 in the x and y-direction respectively, while the interparticle distance was measured as 376 ± 1 and 405 ± 1 in the x and y-direction.

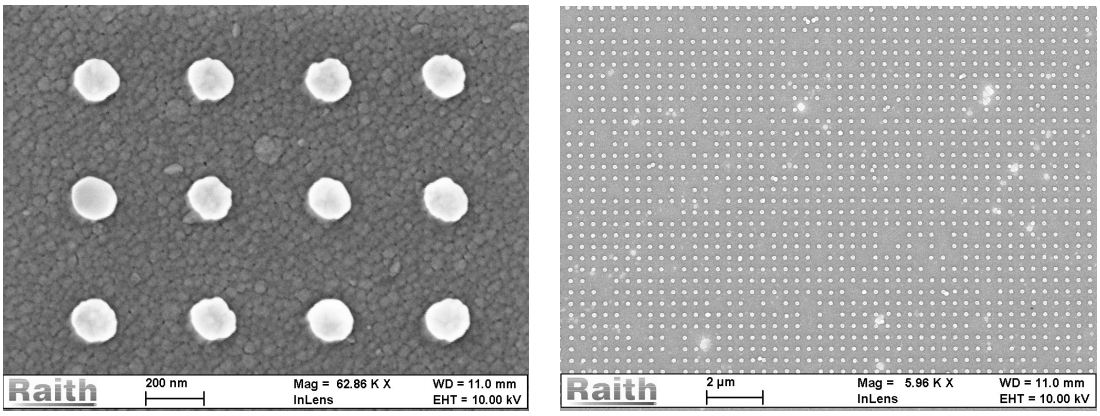

Figure 5.3 SEM images of Au_IPD400. The left picture was used to determine the particle diameter, while the right was used to determine interparticle distance and degree of missing particles. The particle diameters of Au_IPD400 was found to be 158 ± 5 and 148 ± 3 in the x and y-direction respectively, while the interparticle distance was measured as 405 ± 1 and 404 ± 1 in the x and y-direction.

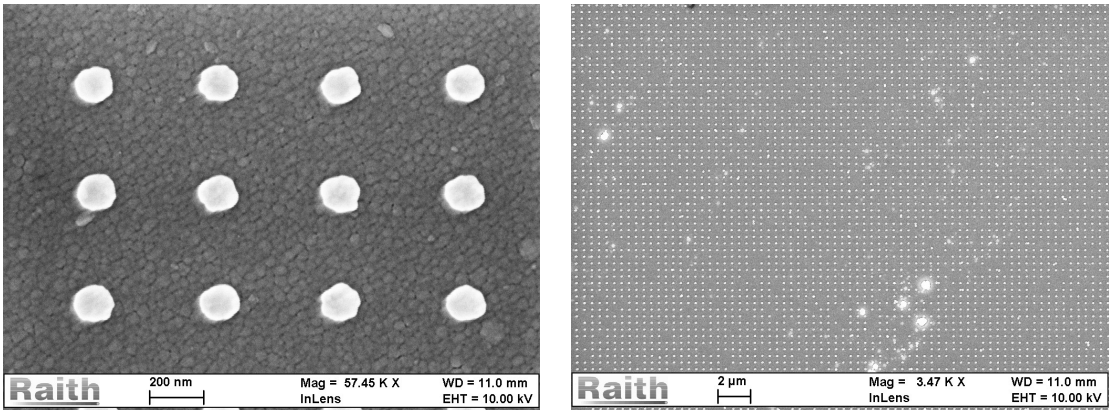

Figure 5.4 SEM images of Au_IPD450. The bright spots on the picture to the right is clusters of the grain-like ITO-structures, and is a part of the ITO-layer. The left picture shows an overview used to determine the interparticle distance and degree of missing particles. The particle diameters of Au_IPD450 was found to be 150 ± 4 and 139 ± 4 in the x and y-direction respectively, while the interparticle distance was measured as 455 ± 2 and 404 ± 1 in the x and y-direction.

The same method was used to characterize a pre-existing set of samples made by Flatabø [43]. These samples are also gold particles on an ITO-covered substrate, and one of the goals of this thesis was to compare the samples produced in this work to the pre-existing set of samples. These samples were investigated using the same method as described above in order to identify the particle sizes and interparticle distances, and the results are presented in Table 5.3. As can be seen from the results, the particles exhibit the same elliptical shape as the ones produced in this work, where they are elongated in the x-direction. All the pre-existing samples had a square lattice with the same interparticle distance in both directions, and the measured interparticle distances were reasonably close to the target distance. One notable difference between sample labelling and particle measurements is that Au_D150_IPD525 actually has an interparticle distance of approximately 500 nm, however this is beneficial because the two samples can now be used to compare the two identical lattices of Au_D150_IPD500 and Au_D150_IPD525 to investigate the degree of consistency of the measurements.

Table 5.3 Particle geometry of pre-existing samples. The difference in diameter between x and y-direction remains, where the particles are larger in the x-direction.

Sample	Diameter x [nm]	Diameter y [nm]	Target diameter xy [nm]
Au_D130_IPD390	129 ± 4	119 ± 4	130
Au_D150_IPD450	139 ± 4	130 ± 4	150
Au_D150_IPD475	159 ± 2	135 ± 4	150
Au_D150_IPD500	148 ± 4	139 ± 6	150
Au_D150_IPD525	151 ± 3	134 ± 5	150

Sample	Int. particle dist. x [nm]	Int. particle dist. y [nm]	Target IPD x [nm]	Target IPD y [nm]
Au_D130_IPD390	393 ± 3	396 ± 4	390	390
Au_D150_IPD450	449 ± 4	452 ± 3	450	450
Au_D150_IPD475	479 ± 2	485 ± 4	475	475
Au_D150_IPD500	506 ± 3	506 ± 2	500	500
Au_D150_IPD525	504 ± 5	507± 6	525	525

The measurements are based on 5 different measurement sites, with three measurements of particle diameter and one measurement of interparticle distance per site. Depicted below are examples of the pictures used to measure these values.

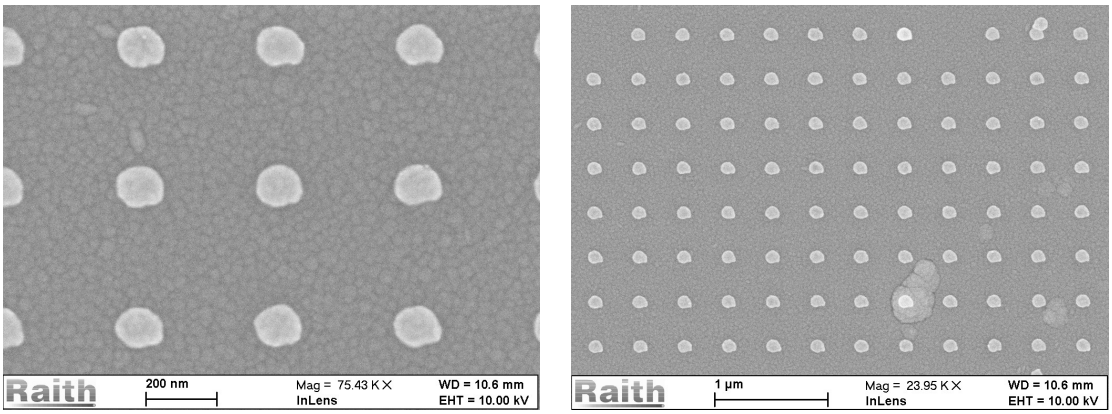

Figure 5.5 SEM-image of au_D130_IPD390. The left picture was used to determine the particle diameter, while the right was used to determine interparticle distance and degree of missing particles. The particle diameters of Au_D130_IPD390 was found to be 129 ± 4 and 119 ± 4 in the x and y-direction respectively, while the interparticle distance was measured as 392 ± 3 and 396 ± 4 in the x and y-direction.

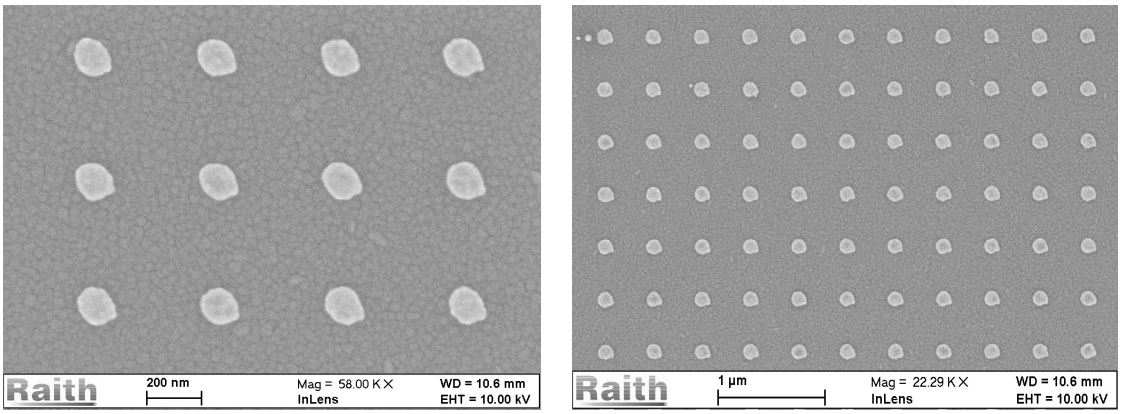

Figure 5.6 SEM image of Au_D150_IPD450. The left picture was used to determine the particle diameter, while the right was used to determine interparticle distance and degree of missing particles. The particle diameters of Au_D150_IPD450 was found to be 139 ± 4 and 130 ± 4 in the x and y-direction respectively, while the interparticle distance was measured as 449 ± 4 and 452 ± 3 in the x and y-direction.

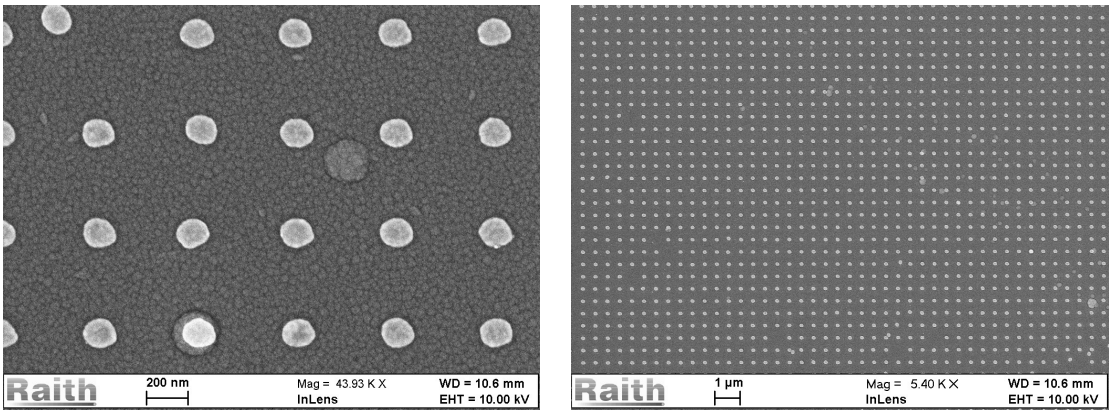

Figure 5.7 SEM-image of Au_D150_IPD475. The left picture was used to determine the particle diameter, while the right was used to determine interparticle distance and degree of missing particles. The particle diameters of Au_D150_IPD475 was found to be 159 ± 2 and 135 ± 4 in the x and y-direction respectively, while the interparticle distance was measured as 479 ± 2 and 485 ± 4 in the x and y-direction.

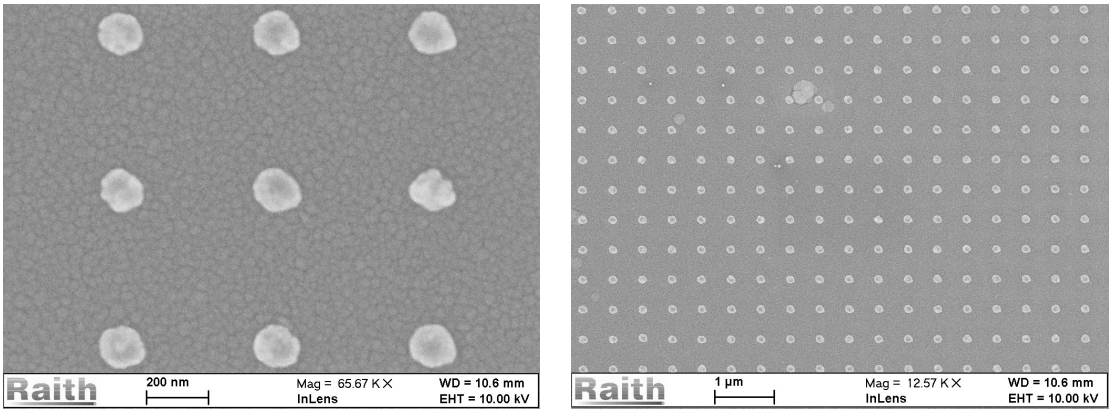

Figure 5.8 SEM-image of Au_D150_IPD500. The left picture was used to determine the particle diameter, while the right was used to determine interparticle distance and degree of missing particles. The particle diameters of Au_D150_IPD500 was found to be 148 ± 4 and 139 ± 6 in the x and y-direction respectively, while the interparticle distance was measured as 506 ± 3 and 506 ± 2 in the x and y-direction.

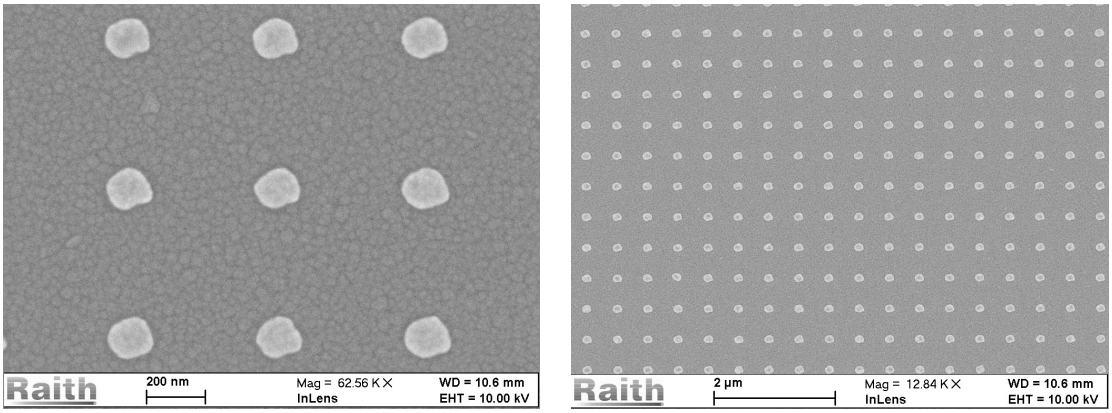

Figure 5.9 SEM-image of Au_D150_IPD525. The left picture was used to determine the particle diameter, while the right was used to determine interparticle distance and degree of missing particles. The particle diameters of Au_D150_IPD525 was found to be 151 ± 3 and 134 ± 5 in the x and y-direction respectively, while the interparticle distance was measured as 504 ± 5 and 507 ± 6 in the x and y-direction.

5.2.1 Sample defects

When producing nanoparticles at a large scale, some structural defects like missing particles and stitching errors are practically inevitable. In general, the number of missing particles were found to be minor, but varying from sample to sample. The exception to this trend is Au_IPD375, where both missing and misplaced particles were fairly prevalent as shown in Figure 5.2. The missing particles can be attributed to different factors in the fabrication process, with the most influential step being the lift-off process. Due to variations in resist thickness from the spin-coating and soft bake processes, the NMP (1-Methyl-2-Pyrrolidone) used to dissolve the resist-layer during the lift-off will vary in effectiveness based on the thickness of the resist layer. The production steps were performed identically for all samples, however some variation is to be expected. The development time and purity of the developer solvent can alter the amount of resist that is dissolved, causing variations in the particles. The temperature of the cleanroom cabinet is controlled by a thermostat, but fluctuations can still occur and affect the spin-coating, development and lift-off processes.

A stitching error was also found between the 100 x 100µm large writefields, where the interparticle distance between the outer particles of the writefield were larger than normal in the x-direction as shown in Figure 5.10. The reason why this occurred was a calculation error in the CAD design file, where the value corresponding to one interparticle distance minus the particle radius (400-150 = 250 nm) should have been subtracted from the total writefield size.

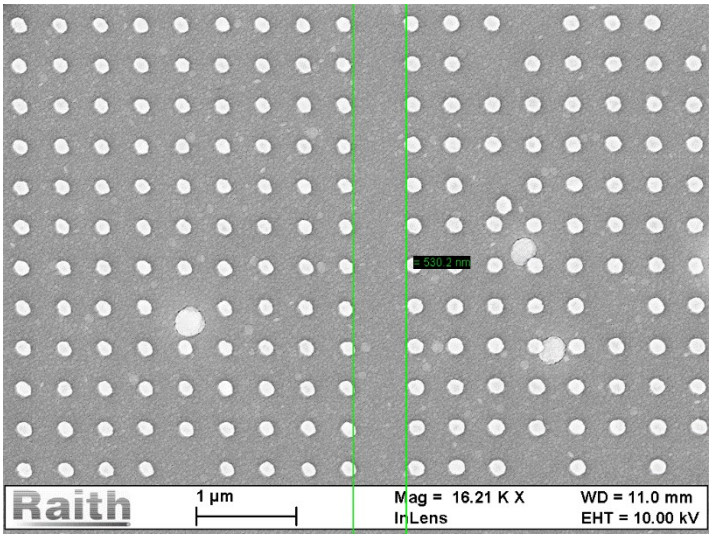

Figure 5.10 Stitching error of Au_IPD400. Note that the measured distance depicted is not representable for the actual error, as you need to measure the lattice vector of the array to get the particle distance. The correct measurement would be to add the particle diameter to the value shown in the picture, netting an interparticle distance of approximately 680 nm.

5.3 Optical characterization

This section describes the results of the optical measurements. The measurements were performed with two different instruments; the Filmetrics thin film analyser (TFA) and a transmission spectrometer setup (TS) with polarised light made in the lab. The polarisation setup was used for the first time in this thesis work. Both instruments are described in detail in section 3. Using these instrument, the transmittance spectra of the samples were obtained, and the extinction spectrum was calculated based on them. The objective of the measurements was to find evidence of selective suppression of the MNPs surface plasmon, determined by the interparticle distance. The TS was equipped with a polarisation filter, which made it possible to distinguish between light polarised across the long or short axes of the particle array, while the TFA use unpolarised light.

5.4 Transmission spectrometer measurements

The transmission spectrometer consists of a tungsten halogen light source guided by an optical fibre, a sample stage, and a beam splitter guiding into a detector and a camera (depicted in Figure 3.5). The detector measures wavelengths of light in the range of 380-1030 nm. Using the SpectraSuite software, the measurements were carried out using the average of a set of 25 scans, each with an integration time of 70 ms. In order to calculate the extinction values of the MNPs as explained in section 2.5, several transmittance intensity spectra were measured; the light source without any sample present, light shining through the ITO layer, and lastly the light transmitted through the particle arrays.

It became apparent that measuring the intensity of the ITO layer as close to the particle arrays as possible was of vital importance to the quality of the spectra, as a measurement performed far away from the arrays did not appear to be representative of the ITO layer situated beneath the particles. This is an indication of an inhomogeneous ITO layer, which in theory could affect the position of the suppression effect [21]. However, because of the transparent nature of the ITO layer, measuring the layer thickness is difficult, which makes quantifying this property challenging. In addition to differences in the thickness of the ITO layer, polarisation direction of the filter had an impact on the extinction magnitude. Therefore, separate measurements of all three spectra were made when changing polarisation direction.

5.4.1 ITO layer extinction measurements

The extinction spectra of the substrate, which includes the fused silica coverslip and the ITO layer, is presented in Figure 5.11. Although they are similar, small changes in the spectra proved to radically change the resulting MNP extinction spectrum. There is also a general trend where the y-polarisation results in a higher extinction than the x-polarisation. This points to that the intensity from the light source vary when the polarisation changes. Although this is indeed the case, this would only affect the intensity measurements, and not the calculated extinction spectra, because the extinction is the fraction of transmitted and incident light intensity, meaning it is independent of the intensity of the incident beam. The different extinction values are therefore thought to be some polarisation dependent interaction between light and either the ITO layer or the silica substrate, and is not yet understood. In all the remaining measurements, these substrate extinctions have been subtracted to obtain the extinction of the particles.

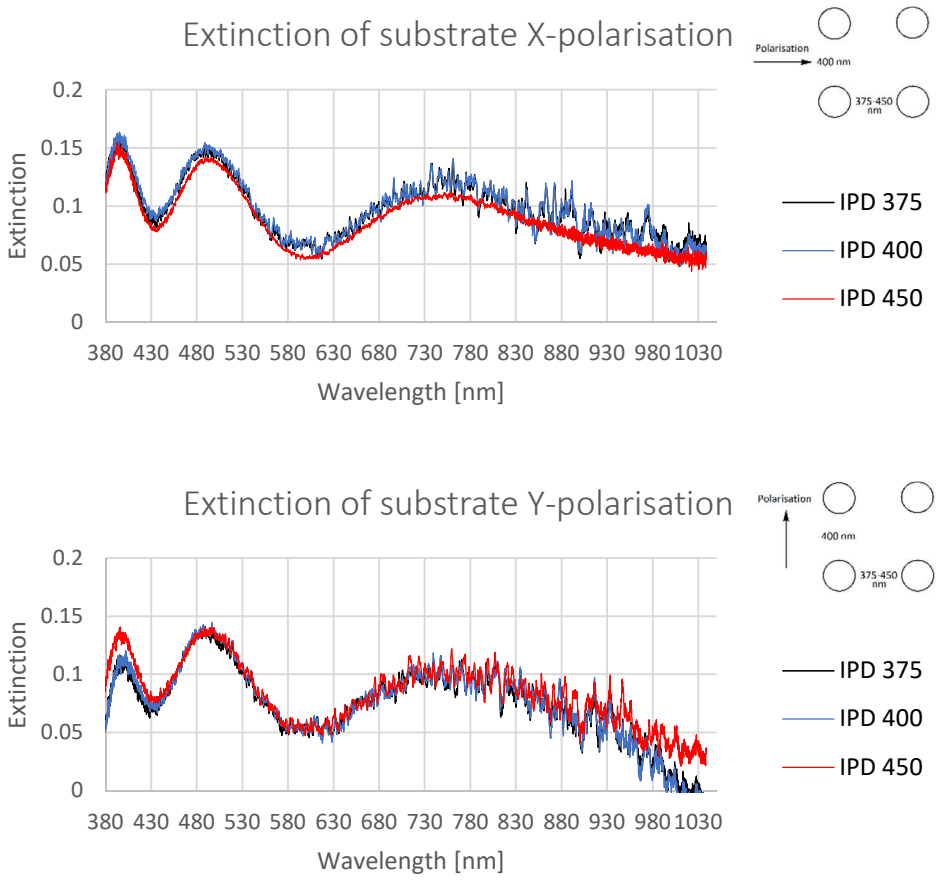

Figure 5.11 Substrate extinction spectra. Note the general trend where the x-polarised light results in approximately a 0.02 lower extinction.

5.4.2 Metal nanoparticle extinction measurements

In this section, the samples produced in this thesis work is examined using both the TS and TFA measuring setups, and compared to pre-existing samples produced by Flatabø [43]. *The expected result is a suppression of the particle LSPR, and that the spectral position of this suppression effect is dependent on the interparticle distance, as explained in section 2.6. The main difference between the TS and TFA is that the TS employs polarised light, while the TFA is unpolarised. All measurements are non-normalized, meaning the extinction values are presented as measured. To separate the samples by name the samples produced in this work is named only by their interparticle distance, due to all the diameters being 150 nm. The previously produced samples include the particle diameter in the sample names.*

General measurement trends

In the following sections the extinction spectrums from all the samples are presented. The expectation, based on the theory outlined in chapter 2, is that parts of the incident light beam will couple into the ITO waveguide, either in TM or TE modes. Each of these waveguide modes are expected to cause a suppression of the metal nanoparticle extinction if within the LSPR resonance, or an enhanced extinction if outside of the LSPR, the former due to destructive interference. The main objective of these measurements is to determine the effect of polarised light on the extinction suppression, and the expectation was to find two extinction dips. This was not the case however, and the resulting spectra exhibit three or four dips rather than two. The following sections include the spectrum as well as comments about peak and dip positions, and a summary with discussion and suggestions as to why the measurements deviate from the theory will be provided in section 5.4.3. For the sake of clarity, a definition of the x and y polarisation directions with respect to the samples are provided in Figure 5.12.

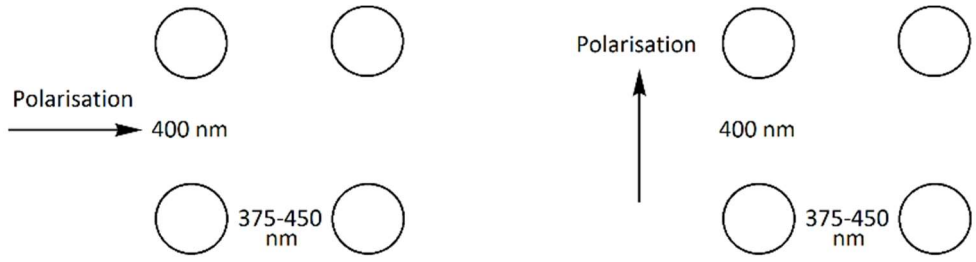

Figure 5.12 Definition of polarisation directions. The left pane depicts x-polarised light, while the right pane shows y-polarised light.

Au_IPD375

The measured particle size in this sample was 160 ± 5 and 141 ± 5 nm, and interparticle distance was 376 ± 1 and 405 ± 1 nm in the x and y directions respectively. The unpolarised spectrum of the TFA represents the superposition between the two excited plasmons of the x and y directions. The x-polarised plasmon is also redshifted compared to the y-polarised, which is expected due to the particles elongation in the x-direction (see section 2.4.1). As previously mentioned, the expected number of dips in the spectrum is two, while in the case of Au_IPD375 the x-polarised measurement shows a total of four dips, and the y-polarised measurement shows three. An interesting feature of the TFA spectrum compared to the polarised measurements is that the TFA spectrum seems to mirror the peaks and dips of the polarised spectrums, but replacing peaks with dips and vice versa. This is illustrated better in the measurements of Au_IPD400 presented in Figure 5.14, and will be referred to as the mirror-effect.

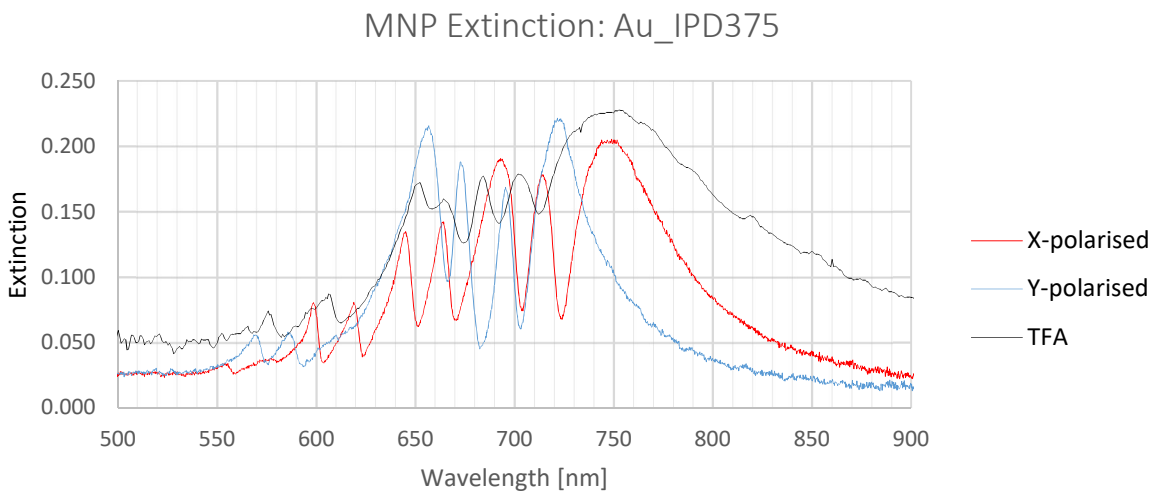

Figure 5.13 MNP extinction of Au_IPD375.

Au_IPD400

The measured particle size in this sample was 158 ± 5 and 148 ± 3 nm, and interparticle distance was 405 ± 1 and 404 ± 1 nm in the x and y directions respectively. In the measurements depicted in Figure 5.15 we see an overlap in the x- and y-polarised spectrums, which is expected as the interparticle distances are 400 nm in both directions. The phenomenon of the TFA-measurements exhibiting opposite dips and peaks as those of the TS measurements is also clearly shown here, especially at the middle dip of approximately 705 nm. There are also only three extinction dips in the TS measurements as opposed to the four dips in the asymmetric samples.

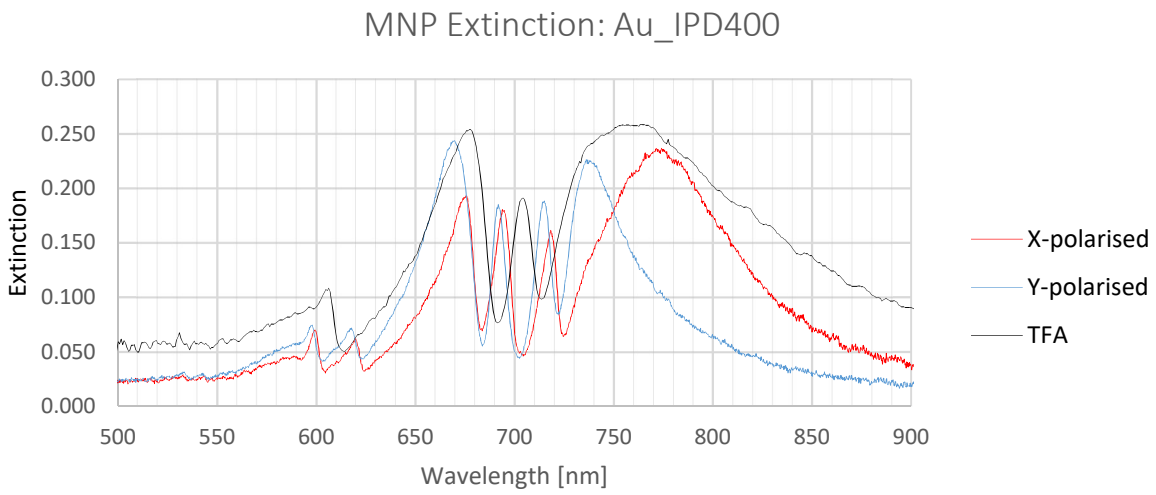

Figure 5.14 MNP extinction of Au_IPD400.

Au_IP450

The measured particle size in this sample was 150 ± 4 and 139 ± 4 nm, and interparticle distance was 455 ± 2 and 404 ± 1 nm in the x and y directions respectively. The most notable feature of this measurement is the two extra peaks to the right of the plasmon (at 770 and 790 nm). These are manifested as peaks because the waveguide modes have energies outside of the LSPR spectral range, and thus manifest as extinction enhancement due to lack of destructive interference as described in section 2.6. It is surprising however that these peaks show up in the y-polarised spectrum, as they are expected to be the same across all samples due to the fact that they have the same interparticle distance in the y-direction. This reinforces the hypothesis that

both polarised spectrums show features from both x and y-polarised light, which will be discussed further in section 5.4.3.

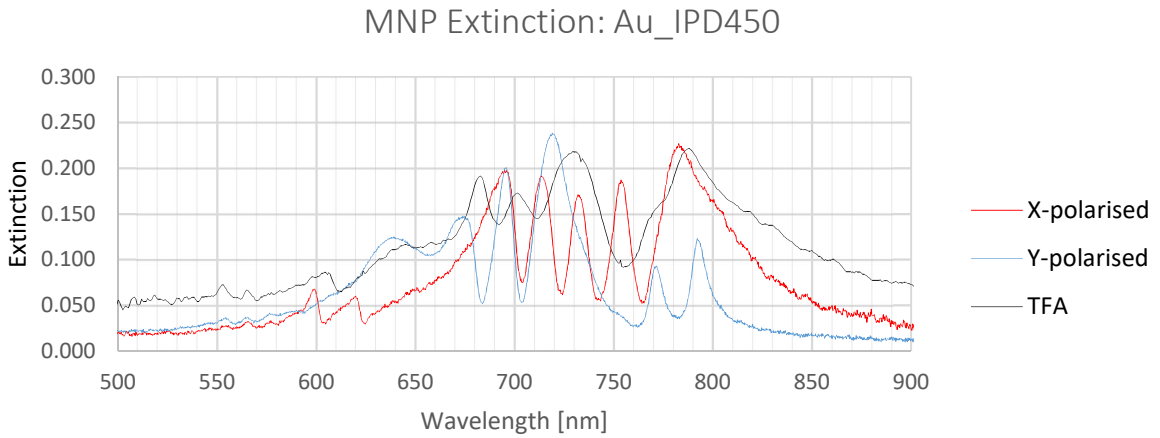

Figure 5.15 MNP extinction of Au_IPD450

Au_D130_IPD390

The measured particle size in this sample was 129 ± 4 and 119 ± 4 nm, and interparticle distance was 393 ± 3 and 396 ± 3.5 nm in the x and y directions respectively. From the TS measurements we see three dips, and a small peak is visible at the middle dip of 770 nm. Because of the symmetrical nature of the sample, it is expected that the polarised spectrums match up, which is indeed the case. The mirror effect is also clearly present, where the TFA spectrum has peaks where the polarised spectrums exhibit dips.

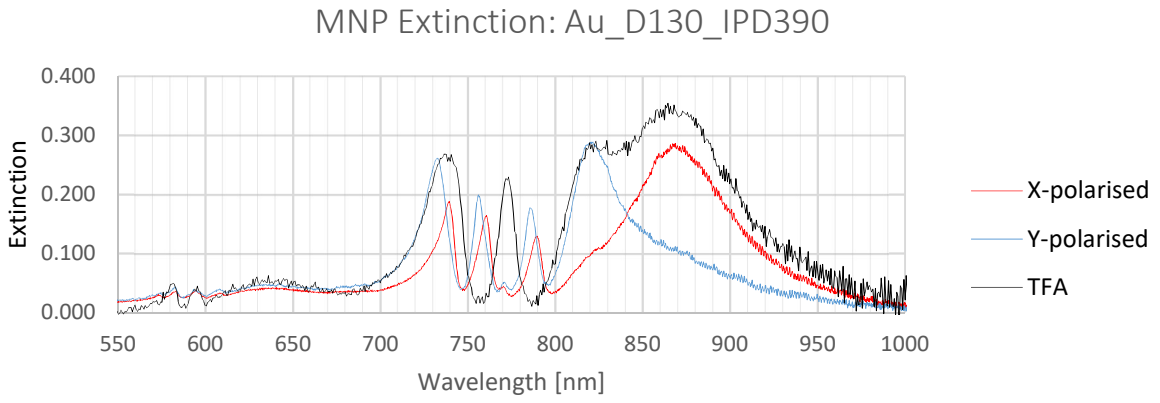

Figure 5.16 MNP extinction of Au_D130_IPD390.

Au_D150_IPD450

The measured geometry of these particles were diameters of 139 ± 4 and 130 ± 4 nm, and interparticle distances of 449 ± 3.5 and 452 ± 2.5 nm in the x and y direction respectively. The measured extinction shows excellent agreement between the polarised and unpolarised plasmon positions and extinction intensity. There is also a broad slope extending out in the spectral range of 715 to 780 nm of the x-polarised measurement. The origin of this broad extinction suppression is unknown, however there is a correlation between the plasmon peak excited by the y-polarised light and this area of suppression, which could indicate that they are affecting each other somehow. This is however pure speculation. The middle dips overlap, which is expected due to the symmetrical nature of the sample.

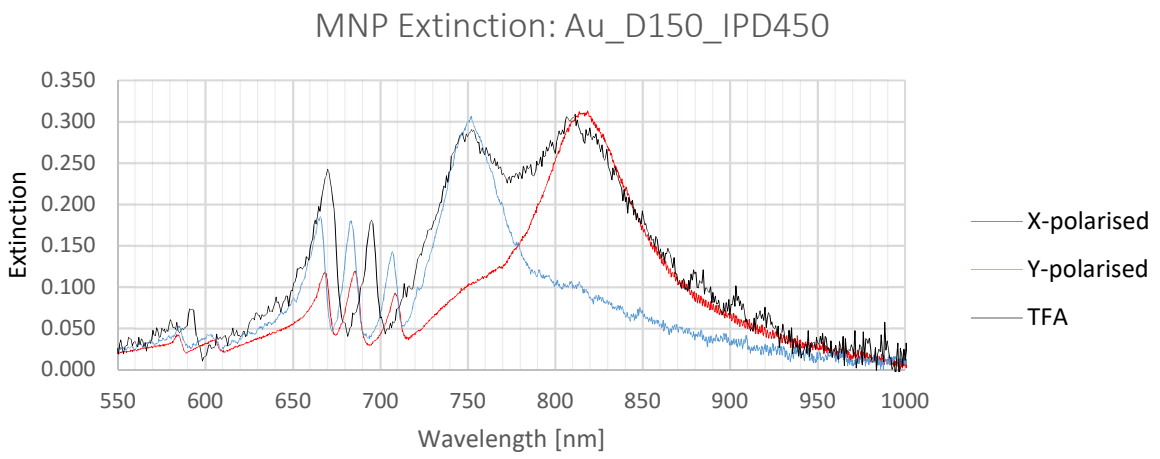

Figure 5.17 MNP extinction of Au_D150_IPD450

Au_D150_IPD475

The measured geometry of these particles were diameters of 159 ± 2 and 135 ± 4 nm, and interparticle distances of 479 ± 2 and 485 ± 4 nm in the x and y direction respectively. The unpolarised TFA measurements correspond well to the sum of the x and y-polarised measurement of the plasmon resonance. The two middle dips of the polarised spectrums are far enough apart that a split appears in the middle. As with all the symmetric samples, the mirror effect is also present, showing a large peak in at 805 nm in the TFA measurements.

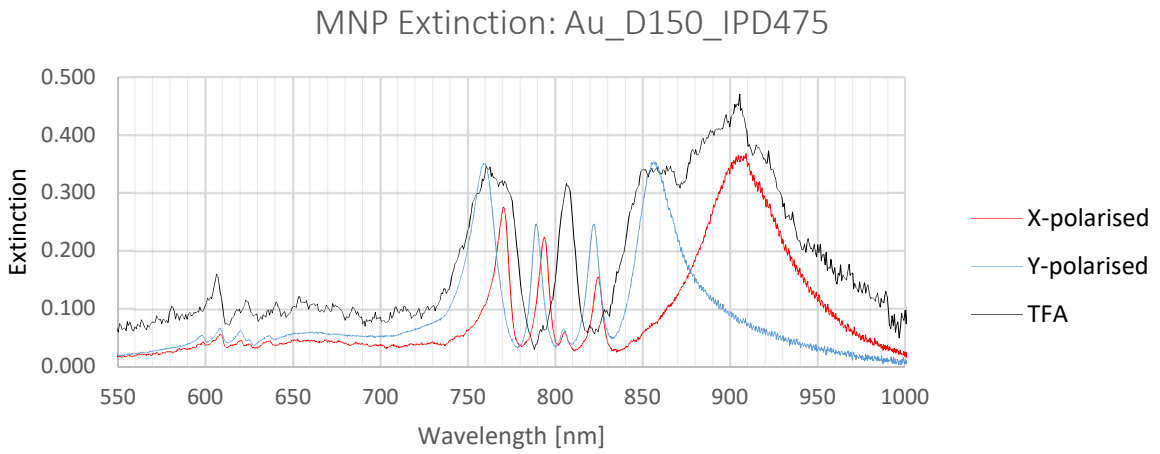

Figure 5.18 MNP extinction of Au_D150_IPD475.

Au_D150_IPD500

The measured geometry of these particles were diameters of 148 ± 4 and 139 ± 6 nm, and interparticle distances of 506 ± 3 and 506 ± 1.5 nm in the x and y direction respectively. The intensity of extinction in the 860-910 nm spectral range is here significantly higher in the unpolarised TFA measurements. The beam spot size of the TS is approximately 0.5 mm in diameter, and therefore it is possible that the polarised measurements were carried out on a part of the sample with less particle surface coverage.

However, the SEM-investigation did not uncover significant areas of missing particles in Au_D150_IPD500, and this phenomenon is not present in the other measurements. Due to the symmetric nature of the sample, the extinction suppression dips are expected to coincide with each other in the polarised measurements, however this is not the case. Three dips are shown in the x-polarised spectrum, which is the expected number when comparing the results of the other samples. However, the y-polarised light exhibits four dips, which indicates a difference in the interparticle distances in the x and y-directions of the sample. This was not observed during the SEM-investigation, and as such the reason for the misalignment of dips is unknown.

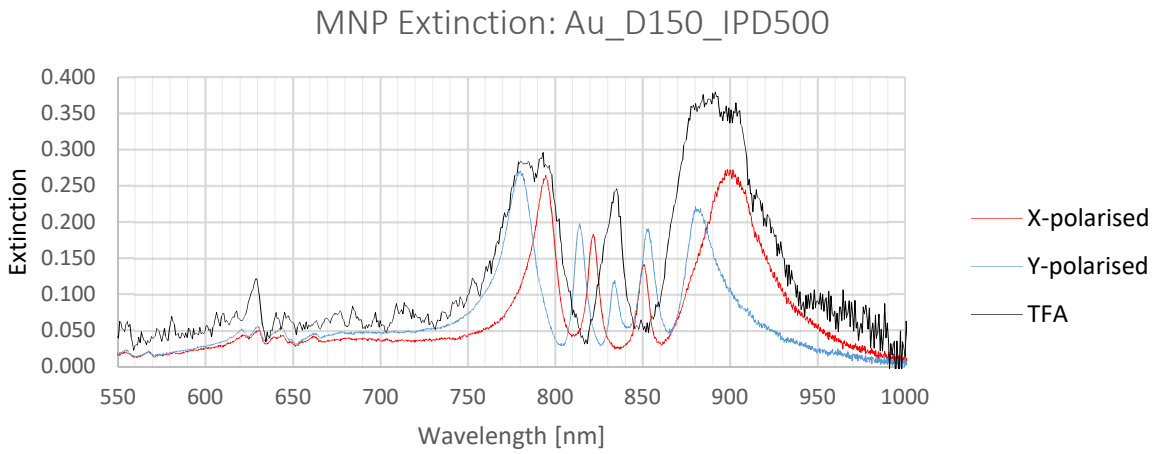

Figure 5.19 MNP extinction of Au_D150_IPD500

Au_D150_IPD525

The measured geometry of these particles were diameters of 151 ± 3 and 134 ± 5 nm, and interparticle distances of 504 ± 5 and 507 ± 5.5 nm in the x and y direction respectively. The particle geometry is as such similar to Au_D150_IPD500, as shown in Table 5.3. The sample name was kept in order to distinguish one from the other. In this case, as opposed to the measurement of Au_D150_IPD500 the x- and y-polarised spectrums coincides, which is expected due to equal interparticle distances in the x- and y-direction. Both polarised spectrums also exhibit a small peak in between the middle dip at approximately 835 nm.

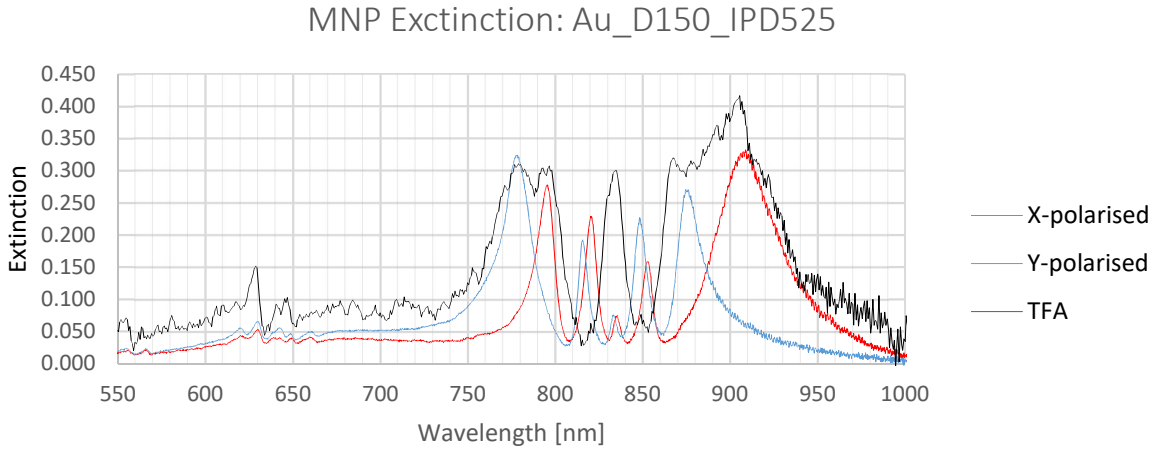

Figure 5.20 MNP extinction of Au_D150_IPD525

5.4.3 Summary of measurements

This section covers a summary and discussion of the measurements, as well as a proposed hypothesis to explain some of the observed spectrum characteristics.

Spectral positions of extinction dips

As previously stated, the expected results were to find two extinction dips (one set) in each of the measured spectra (see section 2.6). However, the results show either three or four dips. A possible explanation for this is that the polarisation filter was not aligned perfectly with the particle array, and because of this contributions from both x- and y-polarised light show up on both measurement spectrums. Given this assumption, there should be double the amounts of expected dips, which is four dips per spectrum. However, the symmetric samples only exhibit three dips instead of four, where the middle dips are widened or in some cases even exhibit a small peak in the middle (see for example Figure 5.20).

The proposed explanation of this is that the middle dip in the symmetric samples in reality are composed of two dips, which cause a broadening of the middle dips and, if far enough apart a small peak between them. This is consistent with the measurements, where all the middle peaks are broadened. The hypothesis is therefore that all the polarised spectrums exhibit four dips, two from each polarisation, where some of the overlap. However, the two sets of dips do not overlap in the symmetric samples. To explain why these two sets are not energetically degenerate, we turn to the properties of the TE and TM waveguide modes.

As illustrated by Figure 2.4, the configuration of the waveguide mode (TE or TM) is determined by the polarisation of the incident light [21]. It is the propagation direction of the waveguide mode that determines if the $\mathbf{k}_{wg}$-vector is defined by the interparticle distances of x or y. This means that y-polarised light couples a TE-mode in the x-direction, and a TM-mode in the y-direction. The opposite is true for the x-polarised light. This, coupled with the fact that TE-waveguide modes have a higher photon energy than TM modes (see section 2.6), leads to the energy differences of the extinction dips. To illustrate, the expected results are as follows:

Table 5.4 Polarisation dependent waveguide mode overview. IPD means interparticle distance. The table is an overview of the direction that the coupled waveguide would affect the sample. For example, with an x-polarised incident beam, the waveguide mode in the x-direction of the particles would be TM.

Polarisation \ IPD direction	**X**	**Y**
X-polarised	TM	TE
Y-polarised	TE	TM

This explains the measurements of the unsymmetrical samples; two dip pairs were present in all measurements, but one of the dip pairs correspond to the x-direction and one to the y-direction, and their energies (waveguide modes) are decided by whether the incident light is polarised in the x- or y direction. To further illustrate this point, a close up of the measurements is shown below

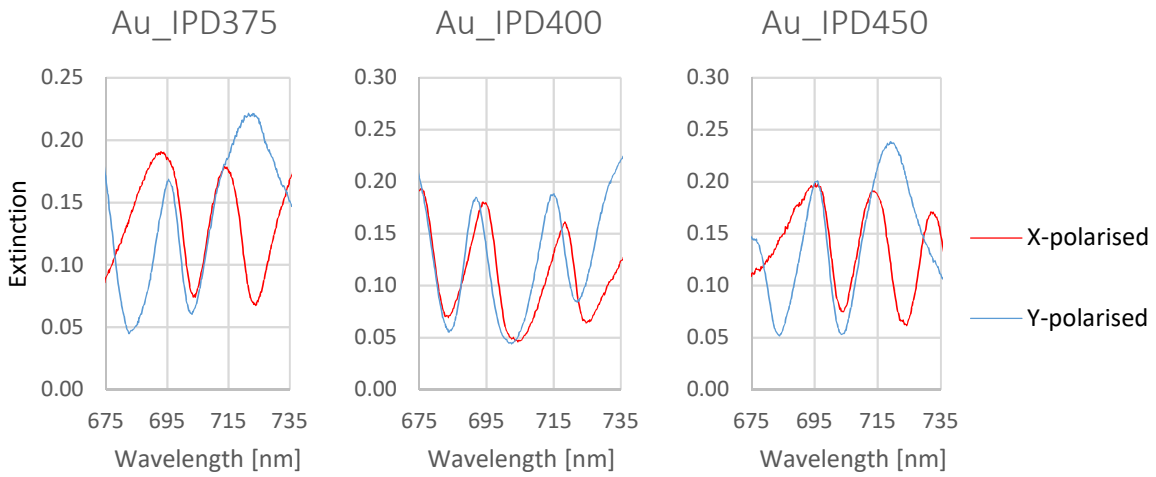

Figure 5.21 Close-up of measurements IPD375-450. Notice the similarities between Au_IPD375 and Au_IPD450. In Au_IPD400 the dips from the particles in the x-direction causes an additional dip to appear at 675 nm. The original measurements are found in Figure 5.13, Figure 5.14 and Figure 5.15.

Figure 5.21 shows a close-up of the measurements of the samples produced in this thesis work, of which two of them (Au_IPD375 and Au_IPD450) are asymmetrical. The spectra of the asymmetric samples match because all the dips have their origin in the waveguide coupled by the particles in the y-direction, and you can see the difference in energy between the TM and TE modes (the x-polarised dips are redshifted relative to the y-polarised dips). In the case of Au_IPD400 which is symmetric, a total of four dip pairs are present, which is the cause of the broadening of the middle dip at 700 nm in both spectrums. This hypothesis would also explain the case of the extra peaks at approximately 770 and 790 nm of Au_IPD450 (see Figure 5.15);

this would be caused by the TE waveguide mode excited by the y-polarised light, which affects the particles in the x-direction. Note however that the energy differences are the opposite of what is expected; the x-polarised light are expected to couple a TE waveguide mode, which has a *higher* photon energy than the corresponding TM mode [21], meaning the x-polarised spectrum should be blue-shifted relative to the y-polarised spectrum. In this case the opposite is observed, however this can be attributed to the fact that the polarisation direction is not clearly defined. It is important to emphasize that this is merely a hypothesis based on the theory available, which is described in section 2.6.

LSPR spectral positions

As shown in Table 5.3 and Table 5.2 displaying the results of SEM particle characterization, the particle samples are all elongated in the x-direction. This should in theory correspond to a red-shift of the LSPR when the incident light beam is polarised in the x-direction (see section 2.4), which is consistently present in the measurements; All the measured samples exhibited a red-shift of the LSPR when measured with x-polarised light. It should be noted that the exact position of the plasmon resonance is hard to evaluate, as this is done by measuring the position of the plasmon peak. The plasmon extinction peak is not defined in these measurements, because of the extinction suppression caused by the coupled waveguide modes. The plasmon positions is therefore roughly evaluated by their spectral start- and ending points.

One major deviation from the expected results is that the plasmons of the previously produced samples are redshifted compared to the samples produced in this work; the LSPs of the previously produced samples lie approximately within the spectral range of 750-950 nm, while the LSPs of the samples produced during this thesis work lie within approximately 650-800 nm. The SEM-investigation of the particles showed that the particles were fairly equal in diameter (about 150 nm), the only exception being Au_D130_IPD390. Given the fact that both particles are placed on ITO substrates and subjected to the same dielectric environment, this shift in plasmonic resonance is attributed to differences in particle height. This could be investigated using for instance atomic force microscopy, but this was not possible within the time frame of this thesis.

The mirror effect and additional peaks

The main difference between the polarised and unpolarised measurements is the inverse orientation of peaks and dips. In the symmetric samples where the interparticle distances are equal in the x- and y-direction, the unpolarised TFA measurements exhibit two broad suppression dips with a thin peak in the middle, which is the opposite of the polarised measurements. One possible explanation for this is that there is destructive interference between the x- and y-polarised waveguide modes, which could explain the increased extinction at the dip positions of the polarised measurements. When considering the samples for use in sensor devices, one of the desired properties is a LSPR peak with a small linewidth (see equation 1.1, section 1.3.3), and all the symmetric samples investigated exhibits an extinction peak with a linewidth of less than 15 nm, without the need for polarised light.

The extra peaks at about 600 nm are attributed to higher order waveguides (see equation 2.34 in section 2.6). The reason why these waveguide modes manifest as extinction peaks rather than dips is because they don't interact by destructive interference with the particle plasmon, as explained in section 2.6. The one exception to this in the measurements is in the case of the y-polarised measurement of Au_IPD450, where the two extinction dips are redshifted into the plasmon itself, manifesting as a broad dip. Given the fact that there are two peaks in all the other samples, a split extinction dip is also expected. Looking closer at the spectrum, as depicted in Figure 5.22, we see that there is no sign of a split in the extinction dip. However, the spectral distance between the supressed areas, approximately between 640 and 670 nm, corresponds well to the spectral distance between the start and end of the two extinction peaks shown in all the other measurements. The reasoning as to why there is no split in this suppression effect is still unclear.

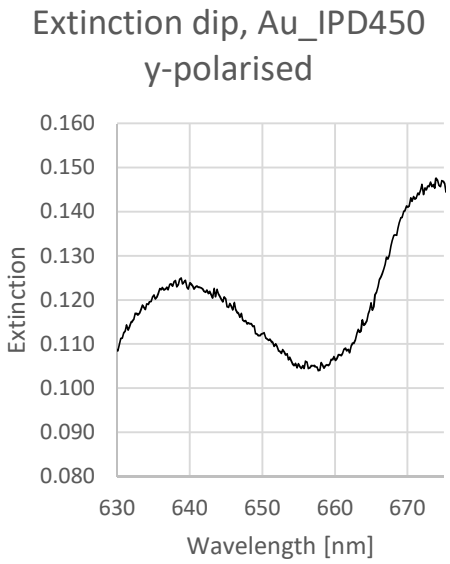

Figure 5.22 Close-up of extinction dip. Taken from Figure 5.15, this shows the suppression effect of the extinction when the coupled light corresponds to the plasmon resonance.

5.5 Comparing the results with existing work

As previously mentioned, the expected waveguide mode photon energies, and by extension the spectral positions of the extinction suppression effect, can be determined by the ITO dispersion relation (see section 2.6). As a consequence, there is a close to linear relationship between the waveguide mode photon energies. The results of the x- and y-polarised measurements of this work and that of Linden et. al [21] is shown in Figure 5.23. Note that the $\mathbf{k}_{wg}$ is calculated using equation 2.34, and that the energies waveguide photon energies was presented in eV in [21] and converted to wavelength (nm) in this representation. It is worth noticing that the x- and y-polarised energies are switched in the measurements of this work compared to that of Linden et. al, further indicating that the polarisation directions of the TS might not be optimal as discussed in section 5.4.3. There is however a clear linear dependency in the measurements, and it is expected that the energies are different, because Linden et. al used a 140 nm thick ITO layer as opposed to the 300 nm layer used in this work, which affects the dispersion relation.

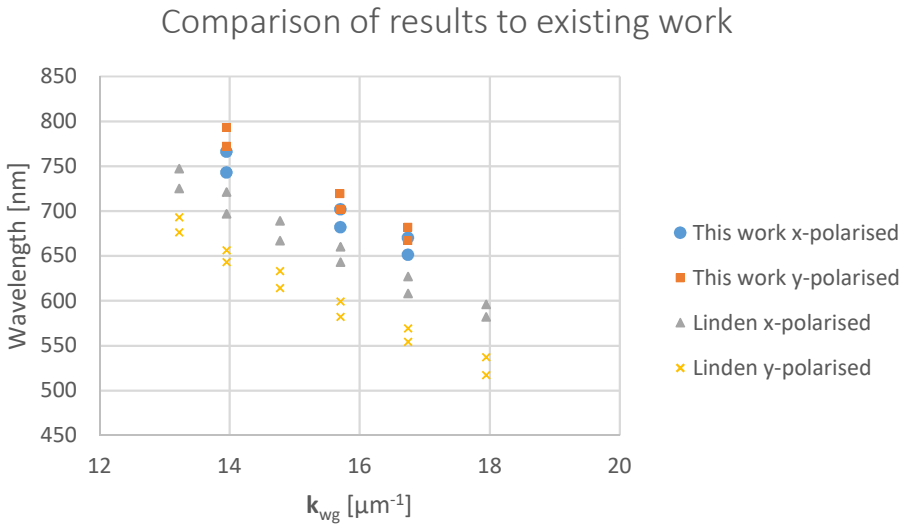

Figure 5.23 A comparison of the results in this work to that of existing work.

6 Conclusion and suggestions for further work

The aim of this thesis was to fabricate large arrays of gold metal nanoparticles and investigate their optical properties using polarised light. The main focus was to investigate the effects of polarised light on the selective extinction suppression of the metal particle localised surface resonance, and evaluate the applicability of this phenomenon in nanoparticle based sensors. The particle arrays were produced by means of electron beam lithography, and the production process was iteratively improved upon to accommodate for poor particle adhesion to the ITO substrate. The employment of a bi-layer resist film improved sample quality to the point where optical measurements could be performed. There is however still room for improvement in the sample quality, and further optimisation of the fabrication parameters would contribute to higher quality samples.

The elongation of the particles in the x-direction should also be looked into; an effort was made to compensate for this effect by employing an elliptical design with the long axis in the y-direction, but this had minimal effect. The particles were examined using transmission spectroscopy with both polarised and unpolarised light, the former using a novel transmission spectrometer. The samples successfully exhibited a suppression effect of the localised surface plasmon, however more suppression dips were found than anticipated by the underlying theory. A hypothesis was suggested that could explain the findings, but this requires further investigation in order to be fully understood.

As for the viability in a nanoparticle based sensor, the results are promising. One of a localized surface plasmon-based sensor is that the linewidth of the plasmon is small; in other words, the peak must be well defined in order to be able to distinguish small spectral changes as the medium surrounding the particles changes. The selective suppression effect significantly reduces the linewidth of the plasmon, however this comes at the cost of a loss of extinction efficiency compared to the plasmon by itself, which could present issues. Polarized light could be employed to this purpose, but more work needs to be done to fully describe the effects of polarised light on the coupled waveguide modes. A suggestion in this regard would be to design a more asymmetrical sample than the ones presented in this thesis, in order to eliminate the contributions from waveguide modes coupled in other directions than the polarisation direction. This could be accomplished by either increasing or decreasing the interparticle distance, where the latter probably would be preferential as a smaller interparticle distance could cause near-field coupling between the LSPRs which could affect measurements.

In addition, to further investigate the viability of a nanoparticle based sensor, optical measurements should be performed on the particle arrays while immersed in mediums of different refractive indices in order to quantify the effect a change in refractive index has on the spectral position of the LSPR. This, along with minimizing the linewidth between the suppressed extinction dips, is key to obtaining a sensitive nanoparticle based sensor.

Bibliography

[1] F. Alam Khan, *Biotechnology Fundamentals*. CRC Press, 2011.

[2] M. Faraday, "The Bakerian lecture: experimental relations of gold (and other metals) to light," *R. Soc.*, vol. 147, pp. 145–181, 1857.

[3] K. L. Kelly, E. Coronado, L. L. Zhao, and G. C. Schatz, "The Optical Properties of Metal Nanoparticles: The Influence of Size, Shape, and Dielectric Environment," *J. Phys. Chem. B*, vol. 107, no. 3, pp. 668–677, 2003.

[4] J. Sire, *Nano!*, 1st ed. Fagbokforlaget, 2009.

[5] D. T. Thompson, "Using gold nanoparticles for catalysis," *Nano Today*, vol. 2, pp. 40–43, 2007.

[6] V. R. A. Holm, M. M. Greve, and B. Holst, "Temperature induced color change in gold nanoparticle arrays: Investigating the annealing effect on the localized surface plasmon resonance," *JVST B*, vol. 34, p. 06K501, 2016.

[7] "nanoComposix nanoparticle manufacturer," 2017. [Online]. Available: http://nanocomposix.com/collections/gold-spheres. [Accessed: 12-Apr-2017].

[8] C. Binns, *Introduction to Nanoscience and Nanotechnology (Wiley Survival Guides in Engineering and Science)*. Wiley, 2011.

[9] T. DiMauro, "Magnetic Induction," 2015. [Online]. Available: http://sdsu-physics.org/NaturalScience100/Topics/3Mind/3magnetism_induction.html. [Accessed: 11-Apr-2017].

[10] I. Rabias, D. Tsitrouli, E. Karakosta, T. Kehagias, G. Diamantopoulos, M. Fardis, D. Stamopoulos, T. G. Maris, P. Falaras, N. Zouridakis, N. Diamantis, G. Panayotou, D. A. Verganelakis, G. I. Drossopoulou, E. C. Tsilibari, and G. Papavassiliou, "Rapid magnetic heating treatment by highly charged maghemite nanoparticles on Wistar rats exocranial glioma tumors at microliter volume," *Biomicrofluidics*, vol. 4, p. 24111, 2010.

[11] C. Altavilla and E. Ciliberto, *Inorganic Nanoparticles: Synthesis, Applications, and Perspectives*. CRC Press, 2010.

[12] N. Lopez, T. V. W. Janssens, B. S. Clausen, Y. Xu, M. Mavrikakis, T. Bligaard, and J. K. Nørskov, "On the origin of the catalytic activity of gold nanoparticles for low-temperature CO oxidation," *J. Catal.*, vol. 223, pp. 232–235, 2004.

[13] D. K. Gramotnev and S. I. Bozhevolnyi, "Plasmonics beyond the diffraction limit," *Nat Phot.*, vol. 4, pp. 83–91, 2010.

[14] S. Rühle, “Tabulated values of the Shockley-Queisser limit for single junction solar cells,” *Sol. Energy*, vol. 130, pp. 139–147, 2016.

[15] M. Iqbal, *An Introduction to Solar Radiation*. 1983.

[16] K. Aydin, V. E. Ferry, R. M. Briggs, and H. a. Atwater, “Broadband polarization-independent resonant light absorption using ultrathin plasmonic super absorbers,” *Nat. Commun.*, vol. 2, p. 517, 2011.

[17] H. Eidsvåg, “A Solar Absorber Based on Metal Nanoparticles,” *Master Thesis, Univ. Bergen*, 2016.

[18] M. E. Stewart, C. R. Anderton, L. B. Thompson, J. Maria, S. K. Gray, J. A. Rogers, and R. G. Nuzzo, “Nanostructured plasmonic sensors,” *Chem. Rev.*, vol. 108, pp. 494–521, 2008.

[19] Z. Yong, D. Y. Lei, C. H. Lam, and Y. Wang, “Ultrahigh refractive index sensing performance of plasmonic quadrupole resonances in gold nanoparticles,” *Nanoscale Research Letters*, vol. 9. p. 187, 2014.

[20] N. Liu, M. Mesch, T. Weiss, M. Hentschel, and H. Giessen, “Infrared perfect absorber and its application as plasmonic sensor,” *Nano Lett.*, vol. 10, pp. 2342–2348, 2010.

[21] S. Linden, A. Christ, J. Kuhl, and H. Giessen, “Selective suppression of extinction within the plasmon resonance of gold nanoparticles,” *Appl. Phys. B Lasers Opt.*, vol. 73, pp. 311–316, 2001.

[22] D. Pines, “Collective Energy Losses in Solids,” *Rev. Mod. Phys.*, vol. 28, pp. 184–198, Jul. 1956.

[23] I. Freestone, N. Meeks, M. Sax, and C. Higgitt, “The Lycurgus Cup --- A Roman nanotechnology,” *Gold Bull.*, vol. 40, pp. 270–277, 2007.

[24] G. Mie, “Beiträge zur Optik trüber Medien, speziell kolloidaler Metallösungen,” *Ann. Phys.*, vol. 330, pp. 377–445, 1908.

[25] R. W. Wood, “On a remarkable case of uneven distribution of light in a diffraction grating spectrum,” *Philos. Mag. Ser. 6*, vol. 4, pp. 396–402, 1902.

[26] U. Fano, “The Theory of Anomalous Diffraction Gratings and of Quasi-Stationary Waves on Metallic Surfaces (Sommerfeld’s Waves),” *J. Opt. Soc. Am.*, vol. 31, pp. 213–222, Mar. 1941.

[27] R. H. Ritchie, “Plasma Losses by Fast Electrons in Thin Films,” *Phys. Rev.*, vol. 106, pp. 874–881, Jun. 1957.

[28] U. Kreibig and P. Zacharias, “Surface plasma resonances in small spherical silver and gold particles,” *Zeitschrift für Phys.*, vol. 231, pp. 128–143, 1970.

[29] S. A. Maier, *Plasmonics: Fundamentals and Applications*. Springer, 2007.

[30] P. Drude, "Zur Elektronentheorie der Metalle," *Ann. Phys.*, vol. 306, pp. 566–613, 1900.

[31] P. Hofmann, *Solid State Physics*, 2nd ed. WILEY-VCH Verlag, 2015.

[32] S. Zeng, D. Baillargeat, H. Ho, and K. Yong, "Nanomaterials enhanced surface plasmon resonance for biological and chemical sensing applications," *Chem. Soc. Rev.*, vol. 43, p. 3426, 2014.

[33] T. R. Jensen, M. L. Duval, K. L. Kelly, A. A. Lazarides, G. C. Schatz, and R. P. Van Duyne, "Nanosphere Lithography: Effect of the External Dielectric Medium on the Surface Plasmon Resonance Spectrum of a Periodic Array of Silver Nanoparticles," *J. Phys. Chem. B*, vol. 103, pp. 9846–9853, 1999.

[34] C. F. Bohren and D. R. Huffman, *Absorption and Scattering of Light by Small Particles*. Weinheim, Germany: Wiley-VCH Verlag GmbH, 1998.

[35] W. Rechberger, A. Hohenau, A. Leitner, J. R. Krenn, B. Lamprecht, and F. R. Aussenegg, "Optical properties of two interacting gold nanoparticles," *Opt. Commun.*, vol. 220, pp. 137–141, 2003.

[36] International Organization for Standardization, "14644-1: Cleanrooms and associated controlled environments–part 1: Classification of air cleanliness.," 2015. [Online]. Available: https://www.iso.org/standard/53394.html. [Accessed: 12-Apr-2017].

[37] M. Stepanova and S. Dew, *Nano-fabrication*. Springer, 2012.

[38] V. R. Manfrinato, J. Wen, L. Zhang, Y. Yang, R. G. Hobbs, B. Baker, D. Su, D. Zakharov, N. J. Zaluzec, D. J. Miller, E. A. Stach, and K. K. Berggren, "Determining the resolution limits of electron-beam lithography: Direct measurement of the point-spread function," *Nano Lett.*, vol. 14, no. 8, pp. 4406–4412, 2014.

[39] M. M. Greve and B. Holst, "Optimization of an electron beam lithography instrument for fast, large area writing at 10 kV acceleration voltage," *JVST B*, vol. 31, p. 43202, Jul. 2013.

[40] A. N. Broers, A. C. F. Hoole, and J. M. Ryan, "Electron beam lithography—Resolution limits," *Microelectron. Eng.*, vol. 32, pp. 131–142, 1996.

[41] J. Du, X. Chen, C. Liu, J. Ni, G. Hou, Y. Zhao, and X. Zhang, "Highly transparent and conductive indium tin oxide thin films for solar cells grown by reactive thermal evaporation at low temperature," *Appl. Phys. A*, vol. 117, pp. 815–822, 2014.

[42] T. O. Håvardstun, "Optical Properties of Metal Nanoparticle Arrays created using Electron Beam Lithography," *Master Thesis, Univ. Bergen*, no. June, 2013.

[43] R. Flatabø, "Optical Properties of Metal Nanoparticle Arrays Created using Electron

Beam Lithography for Solar Cell Application," *Master Thesis, Univ. Bergen*, Jun. 2014.

[44] K.-H. Su, Q.-H. Wei, X. Zhang, J. J. Mock, D. R. Smith, and S. Schultz, "Interparticle Coupling Effects on Plasmon Resonances of Nanogold Particles," *Nano Lett.*, vol. 3, pp. 1087–1090, 2003.

[45] "Chemat Scientific KW-4A Spin Coater manual." [Online]. Available: http://www.chemat.com/chematscientific/docspdf/Spin_Coater_KW-4A_Manual.pdf.

[46] D. Ensminger and F. B. Stulen, *Ultrasonics: Data, Equations and Their Practical Uses*. 2008.

[47] R. Flatabø, A. Coste, and M. M. Greve, "A systematic investigation of the charging effect in scanning electron microscopy for metal nanostructures on insulating substrates," *J. Microsc.*, vol. 265, pp. 287–297, Mar. 2017.